Integrative methylome-transcriptome analysis unravels cancer cell vulnerabilities in infant MLL-rearranged B cell acute lymphoblastic leukemia

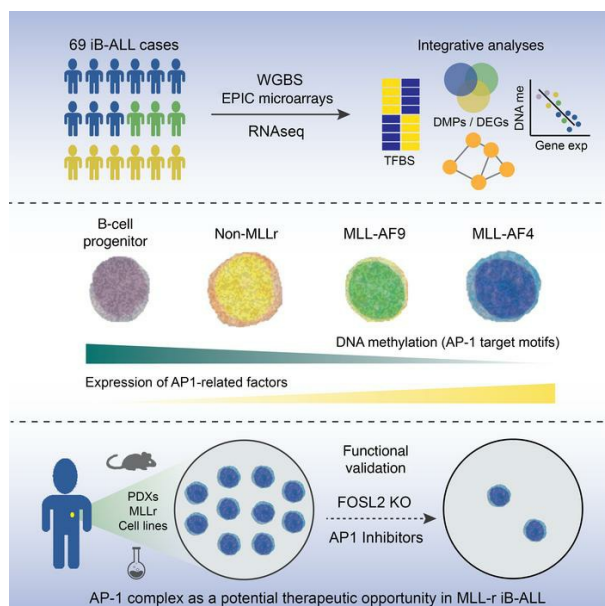Juan Ramón Tejedor, … , Agustín F. Fernández, Pablo Menéndez

Research Article **Genetics** **Oncology**

Graphical abstract

Integrative methylome-transcriptome analysis unravels cancer cell vulnerabilities in infant MLL-rearranged B cell acute lymphoblastic leukemia

Juan Ramón Tejedor,[1,2] Clara Bueno,[3,4,5] Meritxell Vinyoles,[3,4] Paolo Petazzi,[3,4] Antonio Agraz-Doblas,[3,6] Isabel Cobo,[1,3] Raúl Torres-Ruiz,[3,5,7] Gustavo F. Bayón,[1] Raúl F. Pérez,[1,2] Sara López-Tamargo,[1] Francisco Gutierrez-Agüera,[3,5] Pablo Santamarina-Ojeda,[1] Manuel Ramírez-Orellana,[5,8] Michela Bardini,[9] Giovanni Cazzaniga,[9] Paola Ballerini,[10] Pauline Schneider,[11] Ronald W. Stam,[11] Ignacio Varela,[6] Mario F. Fraga,[1,2] Agustín F. Fernández,[1,2] and Pablo Menéndez[3,4,5,12]

[1]Fundación para la Investigación Biosanitaria de Asturias (FINBA), Instituto de Investigación Sanitaria del Principado de Asturias (ISPA), Instituto Universitario de Oncología de Asturias (IUOPA), Hospital Universitario Central de Asturias (HUCA), Universidad de Oviedo, Centro de Investigación Biomédica en Red de Enfermedades Raras (CIBERER), ISCIII, Asturias, Spain. [2]Nanomaterials and Nanotechnology Research Center (CINN-CSIC), Universidad de Oviedo, Asturias, Spain. [3]Josep Carreras Leukemia Research Institute–Campus Clinic, Department of Biomedicine, School of Medicine, University of Barcelona, Barcelona, Spain. [4]Centro de Investigación Biomédica en Red de Cáncer (CIBERONC) and [5]RICORS-TERAV Network, ISCIII, Madrid, Spain. [6]Instituto de Biomedicina y Biotecnología de Cantabria (IBBTEC), Universidad de Cantabria-CSIC, Santander, Spain. [7]Molecular Cytogenetics Group, Human Cancer Genetics Program, Spanish National Cancer Research Centre (CNIO), Madrid, Spain. [8]Hematology Diagnostic Laboratory, Hospital Universitario Niño Jesús, Madrid, Spain. [9]Centro Ricerca Tettamanti, Department of Paediatrics, University of Milano Bicocca, Fondazione MBBM, Monza, Italy. [10]Pediatric Hematology, Armand Trousseau Hospital, Paris, France. [11]Princess Maxima Center for Paediatric Oncology, Utrecht, Netherlands. [12]Instituciò Catalana de Recerca i Estudis Avançats (ICREA), Barcelona, Spain.

B cell acute lymphoblastic leukemia (B-ALL) is the most common childhood cancer. As predicted by its prenatal origin, infant B-ALL (iB-ALL) shows an exceptionally silent DNA mutational landscape, suggesting that alternative epigenetic mechanisms may substantially contribute to its leukemogenesis. Here, we have integrated genome-wide DNA methylome and transcriptome data from 69 patients with de novo MLL-rearranged leukemia (*MLL*r) and non-*MLL*r iB-ALL leukemia uniformly treated according to the Interfant-99/06 protocol. iB-ALL methylome signatures display a plethora of common and specific alterations associated with chromatin states related to enhancer and transcriptional control in normal hematopoietic cells. DNA methylation, gene expression, and gene coexpression network analyses segregated *MLL*r away from non-*MLL*r iB-ALL and identified a coordinated and enriched expression of the AP-1 complex members FOS and JUN and RUNX factors in *MLL*r iB-ALL, consistent with the significant enrichment of hypomethylated CpGs in these genes. Integrative methylome-transcriptome analysis identified consistent cancer cell vulnerabilities, revealed a robust iB-ALL–specific gene expression–correlating dmCpG signature, and confirmed an epigenetic control of AP-1 and RUNX members in reshaping the molecular network of *MLL*r iB-ALL. Finally, pharmacological inhibition or functional ablation of AP-1 dramatically impaired *MLL*r-leukemic growth in vitro and in vivo using *MLL*r-iB-ALL patient–derived xenografts, providing rationale for new therapeutic avenues in *MLL*r-iB-ALL.

Introduction

B cell acute lymphoblastic leukemia (B-ALL) is the most common childhood cancer (1). Current long-term survival rates for pediatric B-ALL approach approximately 85%. However, infant B-ALL (iB-ALL) (<1 year of age) is characterized by an aggressive early clinical manifestation, limited response to current therapies, and poor outcome (2). Chromosomal rearrangements involving the mixed-lineage leukemia gene (*KMTA2*, also known as *MLL*) account for approximately 80% of iB-ALL diagnostics (3), and the clinical outcome of B-ALL patients carrying *MLL* rearrangements (*MLL*r),

especially t(4;11)/*KMT2A-AFF1* (*MLL-AF4*+), is particularly dismal (4). *MLL* encodes for a H3K4 histone methyltransferase (HMT) required for normal hematopoiesis and *HOX* gene expression (5–7). Leukemia transformation by *MLL*r requires the recruitment of the H3K79 HMT Dot1L to the MLL transcriptional complex, rendering a H3K79 methylation pattern in *MLL*r leukemias (8–12).

In iB-ALL, *MLL*r occurs prenatally during embryonic/fetal hematopoiesis (13, 14) and represents an initiating oncogenic driver (15). This, coupled with the extremely short latency, suggests that *MLL*r might be sufficient for leukemogenesis. In line with this, genome-wide DNA-Seq studies in iB-ALL have revealed a silent mutational landscape irrespective of *MLL* status (9, 16, 17), reinforcing the assumption that *MLL*r iB-ALL requires few cooperating mutations for overt leukemia. However, with the exception of a recent work that created a leukemogenic chimeric fusion between human *MLL* and murine *AF4* (18), faithful recapitulation of the *MLL-AF4*+ iB-ALL disease phenotype remains challenging to model (19–23), suggesting that in the absence of

DNA mutations, alternative oncogenic insults may contribute to initiating such infant leukemia (15).

Beyond DNA mutations, changes in gene expression may be caused by epigenetic mechanisms (24–26). It may be plausible that a developmentally restricted specific epigenetic signature in the right fetal cell of origin represents the ideal "soil" for *MLL-AF4*+ to initiate leukemia (27). Alternatively, specific epigenetic alterations may represent "secondary" or "simultaneous" oncogenic events in the pathogenesis of *MLL-AF4*+ iB-ALL. In fact, elegant studies have suggested an important role for DNA methylation in pediatric B-ALL (28–30). In the context of iB-ALL, bisulfite pyrosequencing revealed a specific promoter methylation and hypermethylation of specific microRNAs, distinguishing different subgroups of *MLL*r iB-ALL (31, 32). However, the genome-wide DNA methylation landscape of iB-ALL and its potential relationship with transcriptional programs required for leukemogenesis remains elusive.

Here, we set out to determine the contribution of global DNA methylation to the pathogenesis of iB-ALL through an integrative genome-wide DNA methylome, including whole-genome bisulfite sequencing (WGB-Seq) and transcriptome (RNA-Seq) profiling of 69 *MLL*r and non-*MLL*r iB-ALL leukemias uniformly treated according to the Interfant-99/06 protocol. Our study reveals an iB-ALL–specific gene expression–correlating dmCpG signature and suggests epigenetic control of AP-1 and RUNX members in reshaping the molecular network of *MLL*r iB-ALL by regulating the methylation status of downstream target motifs. Pharmacological inhibition or functional ablation of AP-1 dramatically impairs *MLL*r-leukemic growth in vitro and in vivo, indicating a potential cancer cell vulnerability in *MLL*r iB-ALL. The elucidation of an intricate relationship between DNA methylation and gene expression underlying the pathobiology of *MLL*r and non-*MLL*r iB-ALL opens therapeutic avenues for iB-ALL.

Results

DNA methylation profiling of MLL-AF4+, MLL-AF9+, and non-MLLr iB-ALL. To depict the overall DNA methylation status of iB-ALL, we initially performed WGB-Seq in highly purified (>95%) CD19+CD34+ leukemic blasts from *MLL-AF4*+ (*n* = 2), *MLL-AF9*+ (*n* = 2), and non-*MLL*r (*n* = 2) iB-ALLs and in 2 pools of healthy CD34+CD19+ B cell progenitors (BCPs) as controls (Supplemental Table 1; supplemental material available online with this article; https://doi.org/10.1172/JCI138833DS1). Irrespective of *MLL* status, leukemic blasts from iB-ALL were characterized by a global significantly lower DNA methylation than in healthy BCPs (Figure 1, A and B). Analysis of the *FLT3* gene, a classical *MLL* target overexpressed in *MLL*r iB-ALL (33), confirmed a specific loss of DNA methylation at target gene promoters in *MLL*r iB-ALL, thus validating the WGB-Seq data (Figure 1C). Next, we performed a differential methylation analysis and identified a total of 47,713, 54,409, and 50,127 differentially methylated regions (DMRs), mostly hypomethylated, between healthy BCPs and *MLL-AF4*+, *MLL-AF9*+, and non-*MLL*r iB-ALL patients, respectively (Figure 1D and Supplemental Table 2). DMRs, especially the hypomethylated sites, were enriched in multiple families of DNA repetitive elements (Figure 1E and Supplemental Table 3). WGB-Seq data were validated by DNA

bisulfite pyrosequencing of long interspersed nucleotide element (LINE) and DNA methylation arrays in an extended cohort of *n* = 69 iB-ALLs and *n* = 6 pools of BCPs (Supplemental Figure 1, A and B, and Supplemental Table 4). Taking these data together, iB-ALL is characterized by a global loss of DNA methylation.

To understand the mechanisms underlying a particular epigenomic signature in iB-ALL, we performed a hypergeometric optimization of motif enrichment (HOMER) analysis with the information encoded by either DMRs "specific" for a given iB-ALL subtype or "common" to at least 2 iB-ALL subtypes (Supplemental Figure 2 and Supplemental Table 5). Analysis of hypomethylated DMRs revealed a significant enrichment in PU.1, EBF, SpiB, and ETS for iB-ALL, regardless of *MLL* status, suggesting that these regulators might either trigger a common transcriptional leukemogenic program or regulate normal B cell differentiation. In contrast, hypomethylated DMRs were specifically enriched in the AP-1 family transcription factors (TFs) FOS and JUN and in RUNX family members in *MLL*r iB-ALL.

Different DNA methylation patterns in iB-ALL subtypes according to the genomic location and CpG context. To further capture the epigenetic heterogeneity of iB-ALL, we studied a larger cohort of 37 *MLL-AF4*+, 12 *MLL-AF9*+, and 20 non-*MLL*r iB-ALL using high-content DNA methylation arrays. Six healthy BCPs and naive B cells (34) were analyzed as normal B cell counterparts accounting for DNA methylation changes naturally occurring during B cell differentiation (Figure 2A and Supplemental Table 4). Importantly, DNA methylation arrays and WGB-Seq displayed a very robust correlation (Supplemental Figure 3, A and B). An unsupervised principal component analysis (PCA) segregated iB-ALL methylomes from BCP/naive B cell methylomes (Figure 2B), and a hierarchical clustering of the 10,000 most variable CpG sites distinguished the iB-ALL subtypes, including *MLL-AF4*+ and *MLL-AF9*+ subgroups, suggesting that specific *MLL* fusions might differentially reshape the methylome landscape of iB-ALL (Figure 2C).

We next performed a differential methylation analysis comparing iB-ALLs and healthy naive B cells (34) with healthy BCPs and found 77,596 and 35,157 differentially methylated CpGs (dmCpGs) in iB-ALL and naive B cells, respectively (Figure 2D). Intriguingly, 53% (18,470) of the dmCpGs observed in naive B cells were shared with iB-ALL samples, indicating that they represent methylation changes naturally occurring during B cell differentiation and were therefore subtracted from iB-ALL–specific dmCpGs, providing an iB-ALL–specific dmCpG signature (Figure 2D and Supplemental Table 6). In line with WGB-Seq data, hypomethylated CpGs surpassed hypermethylated CpGs in most of the comparisons (Figure 2D). However, hypermethylated CpGs were substantially abundant in *MLL*r iB-ALL.

To define the overall relatedness among the different iB-ALL subtypes, we performed a global pairwise correlation analysis using the aforementioned iB-ALL–related 77,596 dmCpGs. *MLL-AF4*+ and non-*MLL*r leukemias were the least correlated leukemia subtypes at these aberrant loci (Pearson's correlation, 0.63; Figure 2E). However, while *MLL-AF9*+ leukemias tend to display a higher correlation with *MLL-AF4*+ samples (Pearson's correlation, 0.77), they also shared multiple alterations with non-*MLL*r samples (Pearson's correlation, 0.75), indicating that the *MLL-AF9*+ subtype displays overlapping features with *MLL-AF4*+
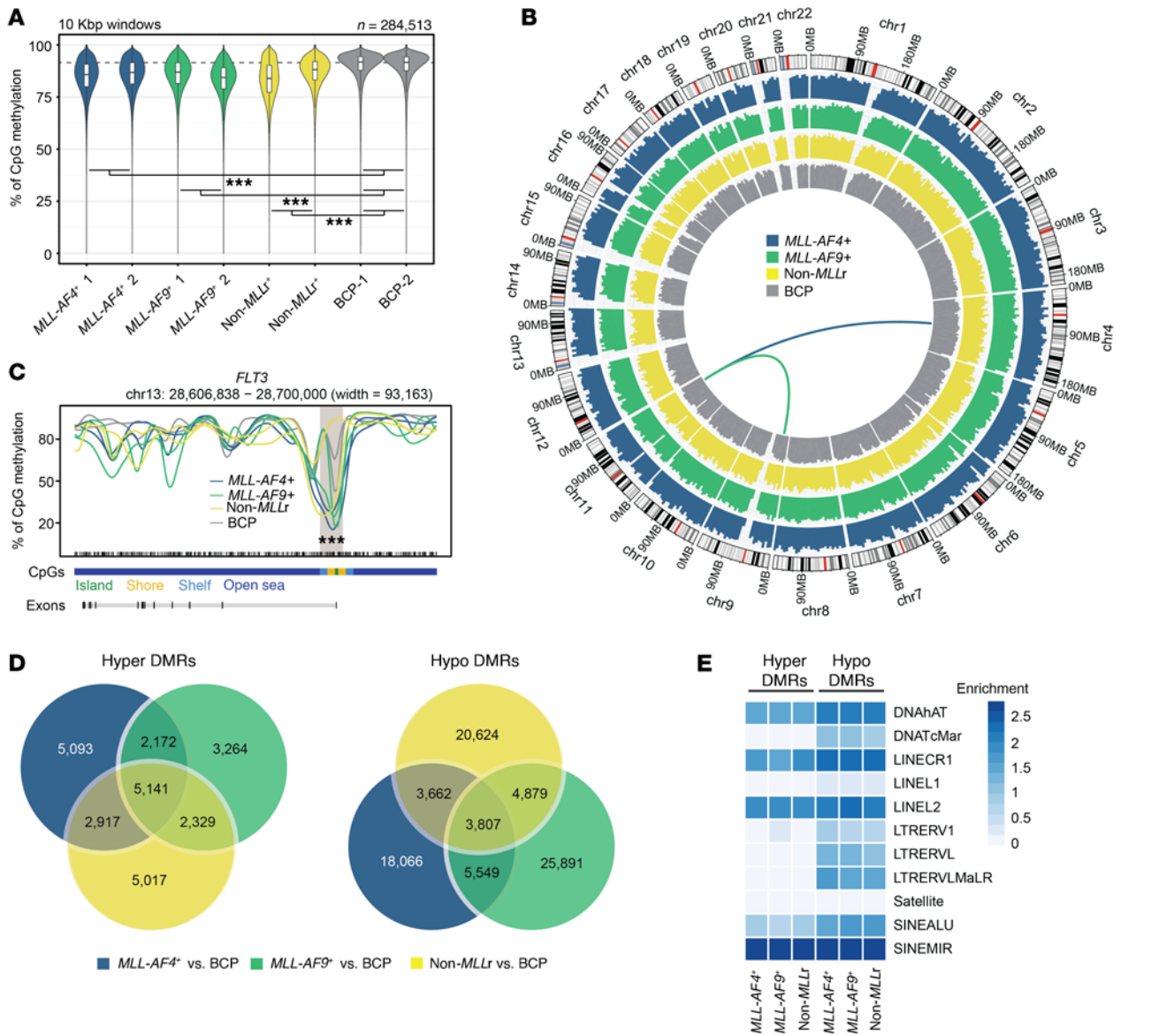
Figure 1. Global DNA methylation status of the different iB-ALL subtypes. (A) Violin plots reflecting the global DNA methylation levels of CpG sites identified by WGB-Seq. Graph represents the percentages of CpG methylation distribution of the genome segmented in 10 Kbp genomic windows. The DNA methylation status significantly differs among all iB-ALL subtypes and the average methylation of healthy BCPs. ***$P < 0.001$, 2-sided Wilcoxon's rank sum test. (B) Circos-plot representation of DNA methylation levels along the genome. CpG methylation was averaged in 10 Mbp genomic windows and the average DNA methylation value for each iB-ALL subtype is represented as a histogram track. Inner lines identify *MLL-AF4*+ (blue) and *MLL-AF9*+ (green) translocation events. (C) Line plots depicting the DNA methylation profile for the *FLT3* gene. The CpG context and the CpG site location are mapped to the corresponding genomic coordinates, as indicated in the lower panels. Areas with significant ($q < 0.05$) differential methylation between *MLL-AF4*+/*MLL-AF9*+ and non-*MLL*r iB-ALL or healthy BCPs methylomes are shaded. ***$P < 0.001$. (D) Venn diagrams representing the total number of DMRs with consistent hyper- or hypomethylation changes for each of the indicated comparisons. (E) Heatmap indicating the log$_2$ odds ratio enrichment of different DNA repetitive regions for significant hyper- or hypomethylated DMRs, respectively ($q < 0.05$).

and non-*MLL*r iB-ALLs. A detailed inspection of the genomic distribution of the dmCpG sites revealed an enrichment of hypomethylated CpGs at open sea locations and intronic regions, while hypermethylated CpGs were enriched in CpG islands, CpG shores, and promoter areas, regardless of the iB-ALL subtype (Figure 3, A and B; statistics available in Supplemental Table 7). Of note, hypermethylated CpGs at CpG islands and promoter regions were more enriched in *MLL-AF4*+ iB-ALL than in *MLL-AF9*+ and non-*MLL*r iB-ALL subgroups, defining a methylome

pattern specific for *MLL-AF4*+ iB-ALL. Healthy naive B cells displayed no substantial enrichment of hypermethylated CpGs at either CpG islands or promoter regions (Figure 3, A and B), indicating that the dmCpG context/location observed in iB-ALL differs from that ascribed to normal B cell differentiation.

We next performed a transcription factor binding site (TFBS) enrichment analysis to predict the involvement of potential TFs enriched in dmCpGs. We used the Gene Transcription Regulation Database (GTRD), which includes the most complete
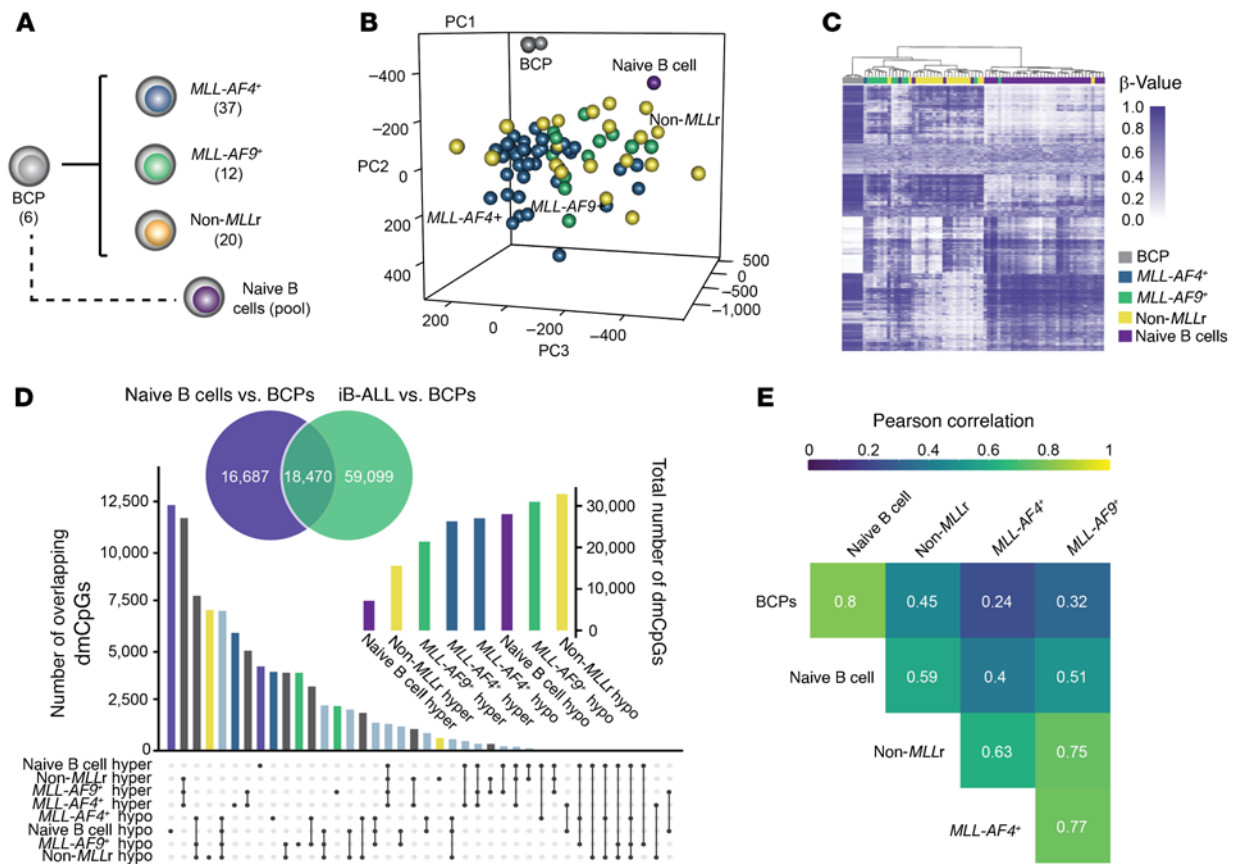
Figure 2. Identification of differentially methylated sites in iB-ALL subgroups. (**A**) Schematic indicating the number of samples analyzed with the Human MethylationEPIC microarray platform. (**B**) PCA for 758,932 CpG sites across all samples included in the DNA methylation study. (**C**) Heatmap representation depicting the methylation status of the 10,000 most variable CpG sites (*y* axis) for the different iB-ALL samples, BCPs, and naive B cells (*x* axis). (**D**) Barplot displaying the number of common (black) and specific (colored) significantly hyper- or hypomethylated CpG sites observed in the indicated comparisons (FDR < 0.05, mean β difference > 0.25). Venn diagram represents the number of overlapping dmCpGs between naive B cells and iB-ALL (β > 0.25). dmCpGs overlapping naive B cells and iB-ALL samples were discarded for downstream analyses because they represent methylation changes naturally occurring during B cell differentiation. The inset shows the total number of hyper- and hypomethylated CpG sites observed in each condition. (**E**) Pairwise Pearson's correlation analysis indicating the degree of similarity between the different sample groups. A total of 77,596 dmCpGs observed at any iB-ALL vs. BCP condition were used for proper comparisons, and all comparisons were statistically significant (*P* < 0.001).

collection of uniformly processed TF ChIP-Seq data available to date (35). In line with WGB-Seq data, analysis of hypomethylated CpGs revealed a significant differential enrichment in *MLL-AF4*+ iB-ALLs for the AP-1 family TFs FOS and JUN (Figure 3C and Supplemental Table 8), suggesting they represent MLL-*AF4*+–specific differentially hypomethylated TFBS.

Aberrant DNA methylation in iB-ALL is associated with a distinctive repertoire of chromatin signatures. To unveil the potential functional implications of aberrant DNA methylation in iB-ALL, we performed a comprehensive region set enrichment analysis by using 6 publicly available histone data sets (H3K4me1, H3K4me3, H3K27ac, H3K27me3, H3K36me3, H3K9me3) comprising a total of 5 reference B-lineage hematopoietic epigenomes from the Roadmap and ENCODE epigenome consortia (36, 37). We found a differential enrichment of iB-ALL–specific, but not normal B cell–specific, hypermethylated CpGs at locations decorated with the H3K4me3 mark (Figure 4A and Supplemental Table 9). This was more evident in *MLL-AF4*+ iB-ALL. Hypomethylated CpGs were not differentially enriched in iB-ALL for any of the histone marks analyzed (Figure 4A).

Given the complexity of the histone code, its widespread distribution, and the plausible colocalization of some of these histone marks, we next performed an enrichment analysis based on chromatin segmentation data to facilitate the interpretation of the potential role of these leukemia alterations in normal tissue. This type of analysis integrates histone mark information from the aforementioned tissues in order to fractionate the genome into functionally related chromatin states (38). The functional distribution of both hyper- and hypomethylated CpG sites differed between iB-ALL subgroups and normally differentiated B cells (Figure 4B and Supplemental Table 10). Hypermethylated CpG sites were significantly enriched in iB-ALL at genomic locations associated with flanking and bivalent transcription start sites (TSSs) (states 2, 4, 14). These enrichments were more consistent for *MLL-AF4*+–specific hypermethylated CpGs. In contrast, DNA hypermethylation enrichment at enhancer regions (states 9–11) associated with normal B cell differentiation was lost in iB-ALL, suggesting that the precise control of these regulatory elements is impaired in iB-ALL, regardless of *MLL* status. Hypomethylated CpG sites
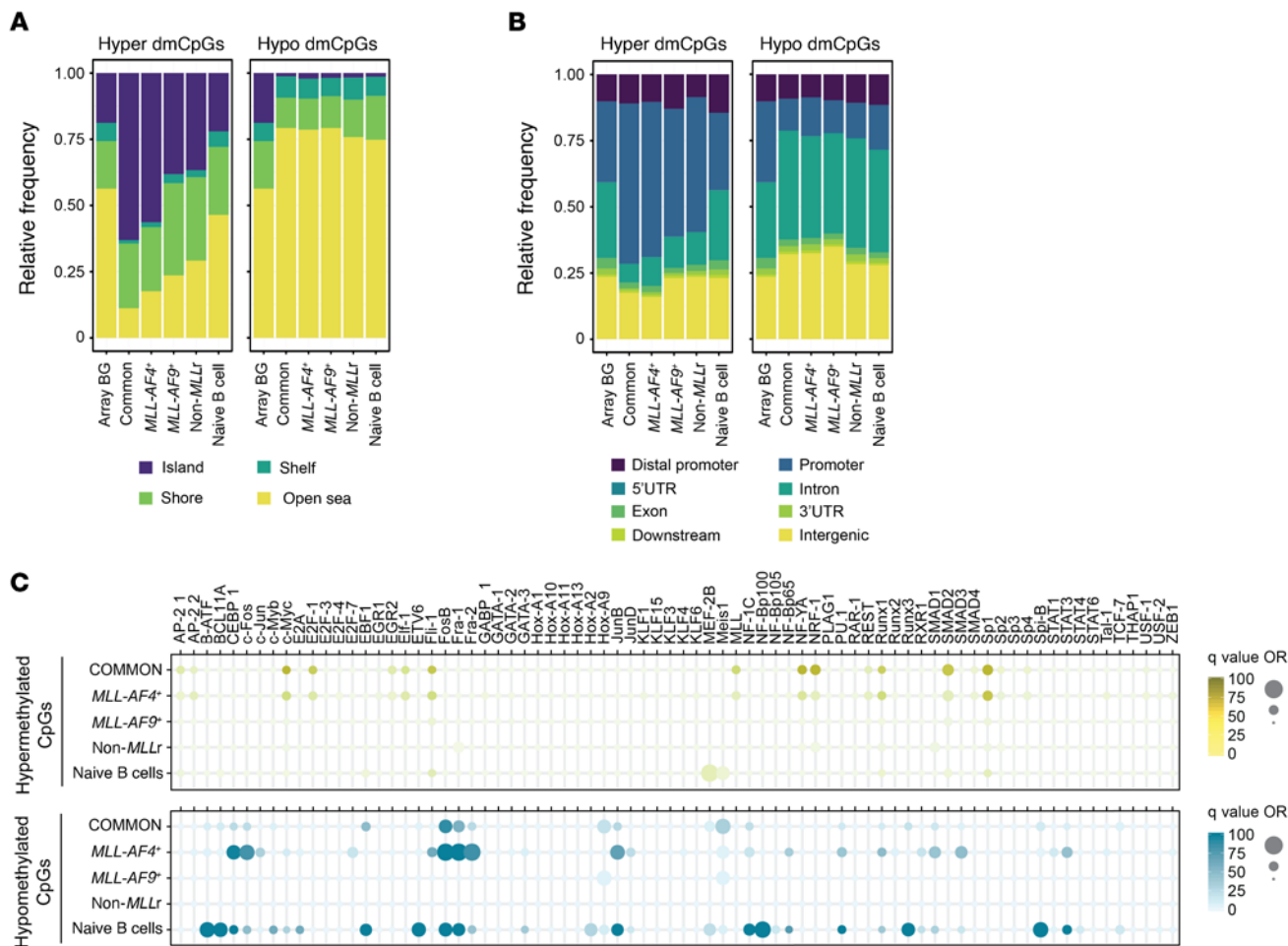
Figure 3. Different DNA methylation patterns in iB-ALL subgroups according to the genomic location and CpG context. (**A** and **B**) Stacked barplots depicting the relative frequency of significant hyper- or hypomethylated CpGs in relation to their CpG context (**A**) or CpG location (**B**). (**C**) Bubble plots showing enrichment of TFBS under the indicated conditions as determined by the information obtained from the GTRD database. Top (yellow bubbles) and bottom (blue bubbles) graphs represent TFBS enriched in hyper- and hypomethylated CpGs, respectively. Bubble color denotes statistical significance ($-\log_2$ adjusted P value). Dot size indicates the $\log_2$ or enrichment of a particular TFBS data set as compared with the background distribution of the EPIC platform.

were also significantly enriched in *MLL*r iB-ALL at genomic locations associated with repressed polycomb elements (states 17, 18; Figure 4B). In addition, a differential enrichment of DNA hypomethylation at enhancer regions (states 7, 8) was observed between iB-ALL subgroups (Figure 4B).

As remodeling of enhancer repertoires plays a key role in the establishment of B cell identity (39), we hypothesized that aberrant enhancer methylation may act as a proxy defining the differentiation status/blockage of iB-ALL. A hierarchical clustering of iB-ALL patients using the naive B cell–specific 361 dmCpG probes from the Human MethylationEPIC platform, which overlap with B cell–specific enhancers from the Enhancer Atlas, segregated *MLL-AF4*+ from *MLL-AF9*+ and non-*MLL*r iB-ALL patients (Supplemental Figure 4 and Supplemental Table 11). Of note, when the average DNA methylation status of the different iB-ALL groups was compared with that of healthy naive B cells, *MLL-AF4*+ and *MLL-AF9*+ iB-ALL displayed a lower correlation than non-*MLL*r iB-ALL, suggesting that *MLL*r iB-ALL are intrinsically defined by a less differentiated B phenotype. Collectively, aberrant DNA methylation seems functionally associated

with different molecular mechanisms involved in the epigenetic remodeling of the distinct iB-ALL subtypes.

The transcriptional program of MLLr iB-ALL is governed by members of the AP-1 complex. Aberrant DNA methylation in iB-ALL associates to the function of chromatin states related to transcriptional control (Figure 3B). To identify relevant cellular pathways displaying transcriptional changes, we next performed a comprehensive transcriptomic analysis of iB-ALL patients ($n = 40$) and healthy BCPs ($n = 5$) from whom paired RNA-Seq DNA methylation data were available (Figure 5A). An unsupervised PCA of the RNA-Seq data readily distinguished iB-ALL patients from healthy naive B cells and BCPs (Figure 5B). Hierarchical clustering based on DNA methylation data was more homogeneous than that based on gene expression, particularly for *MLL-AF4*+ iB-ALL (Figure 5C), as gene expression clustering yielded 2 separate subgroups in *MLL-AF4*+ patients. However, both DNA methylation and gene expression could generally cluster non-*MLL*r apart from *MLL*r patients, indicating that both the methylome and transcriptome landscape of non-*MLL*r and *MLL-AF4*+ iB-ALL are differentially governed.
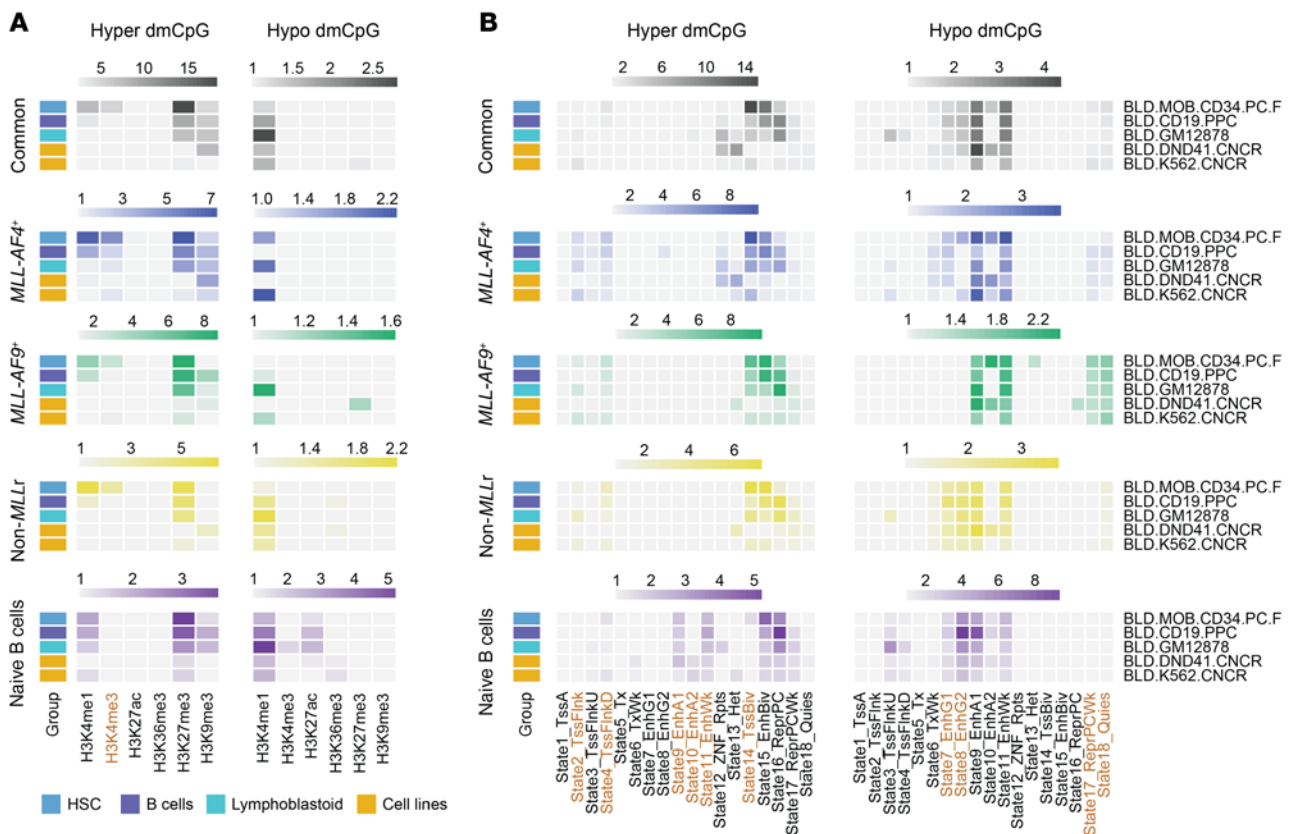
Figure 4. Aberrant DNA methylome in iB-ALL is associated with alterations at particular chromatin states. (**A**) Heatmaps displaying histone mark enrichment analyses of hyper- and hypomethylated CpGs specific for naive B cells, each iB-ALL subtype. or common to a least 2 iB-ALL subtypes, as compared with healthy BCPs. Color scales represent odds ratio of significant dmCpGs obtained in previous analyses across 6 common histone modifications from the NIH Roadmap Epigenome consortium as compared with the background distribution of the Human MethylationEPIC platform. Legend indicates the type of B-lineage hematopoietic data sets used for comparisons. (**B**) Heatmaps representing chromatin state enrichment analyses of hyper- and hypomethylated CpGs in the aforementioned conditions. Color ranges indicate the odds ratio of the significant dmCpGs observed across 18 chromatin states obtained from the NIH Roadmap Epigenome consortium.

We next performed a differential expression analysis of *MLL-AF4*+, *MLL-AF9*+, non-*MLL*r iB-ALLs, and naive B cells (Supplemental Table 12). Our pipeline identified 5170 and 3919 differentially expressed genes (DEGs) specific for iB-ALL and naive B cells, respectively (Figure 5D). *MLL-AF4*+ iB-ALLs displayed a larger expression variability (Figure 5E), consistent with the gene expression heterogeneity observed in the hierarchical clustering (Figure 5C), indicative of distinct molecular subgroups within *MLL-AF4*+ iB-ALL patients (9). To explore the molecular networks underlying the transcriptional rewiring of iB-ALL, we performed a gene coexpression network analysis using the 663 most variable genes from the RNA-Seq and found 3 substantially different gene expression modules (Figure 5F and Supplemental Figure 5A). Modules 1 and 2 were enriched in *MLL-AF4*+ and *MLL-AF9*+ subgroups and barely represented in healthy naive B cells and BCPs, while module 3 mainly distinguished *MLL-AF4*+ iB-ALL from *MLL-AF9*+ and non-*MLL*r iB-ALL (Figure 5F). A detailed inspection of these modules revealed a differential gene set enrichment of gene ontology categories related to cell activation, inflammatory response, and cell division for modules 1, 2, and 3, respectively (Supplemental Figure 5, B and C). In addition, module 2 showed a significant enrichment of gene sets related to NF-κB, p53, and STAT signaling

pathways, while module 3 displayed an enrichment of gene sets associated with G2M checkpoint, E2F targets, and mitotic spindle. A different set of TFs was coexpressed in each module (Supplemental Figure 5,D–F). Importantly, module 2, which best segregated *MLL*r iB-ALLs from non-*MLL*r iB-ALLs and normal naive B cells and BCPs, showed a coordinated and enriched expression of FOS and JUN, TFs of the AP-1 complex (Supplemental Figure 5E), consistent with the significant enrichment of hypomethylated CpGs in FOS and JUN for *MLL*r iB-ALL, indicating that an epigenetic control of these AP-1 members may contribute to the pathogenesis of *MLL*r iB-ALL.

Integrative analysis reveals a gene expression–correlating dmCpG signature and an epigenetic control of AP-1 members in MLLr iB-ALL. We used ELMER (40) to integrate paired DNA methylation and RNA-Seq data in iB-ALL. ELMER correlations were calculated using those dmCpGs specific for a given iB-ALL subtype or common for iB-ALL (shared by > 2 iB-ALL subgroups), and all the genes expressed in the RNA-Seq (Figure 6A). Up to 10%, 17%, 33%, and 25% of the common, *MLL-AF4*+, *MLL-AF9*+, or non-*MLL*r dmCpGs, respectively, showed a robust correlation with gene expression (Supplemental Table 13). To facilitate data interpretation, we focused on those correlations supported by the classical model of epigenetic regulation and found that DNA
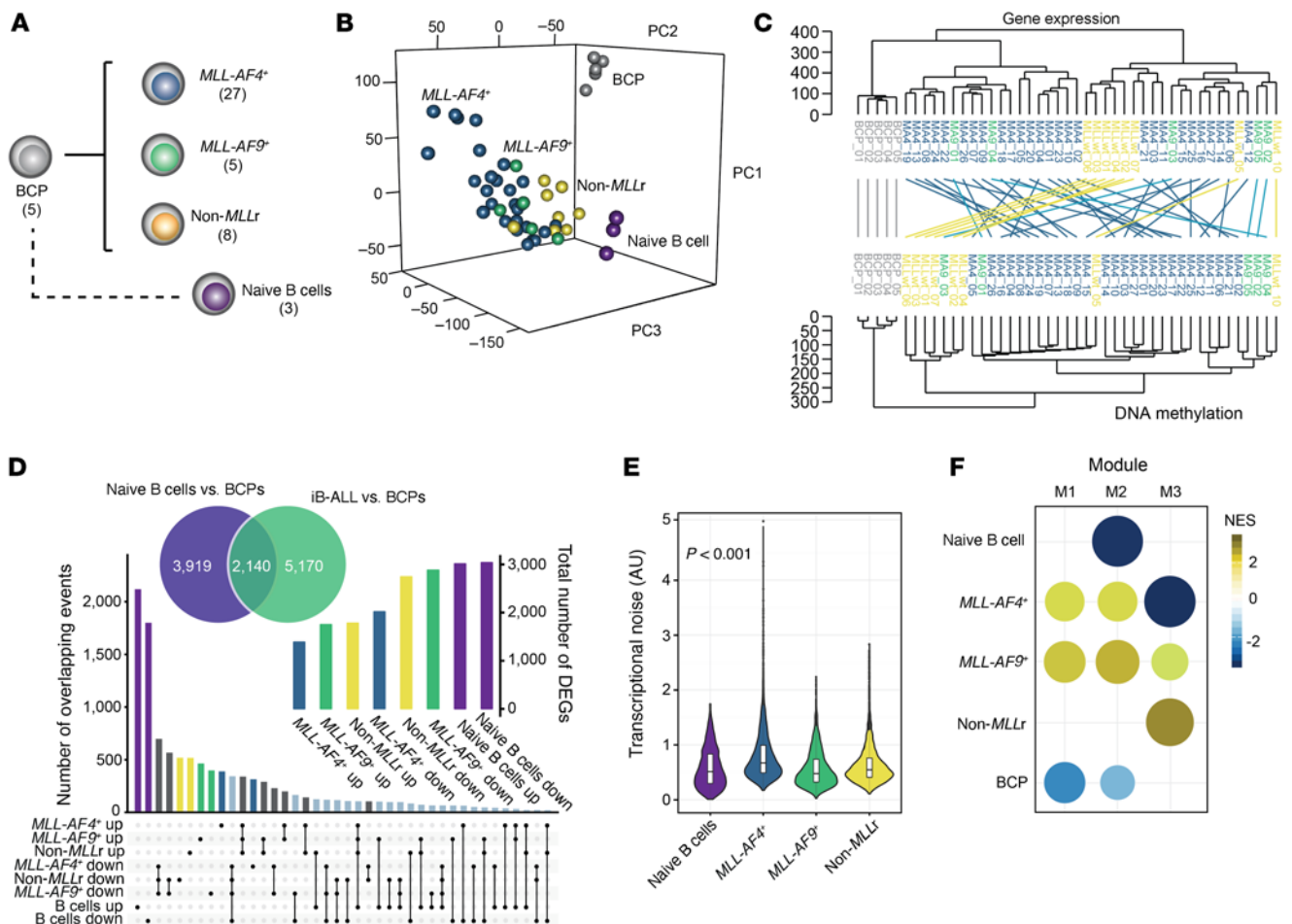
Figure 5. Gene coexpression network analysis reveals the AP-1 complex members JUN and FOS as potential pathogenic contributors in MLLr iB-ALL. (**A**) Schematic depicting the number of samples analyzed by RNA-Seq. (**B**) PCA generated from the gene expression matrix ($\log_2$ fragments per kilobase of transcript per million mapped reads [FPKM] values) across all samples analyzed by RNA-Seq. (**C**) Tanglegram representation of the cluster relationship between paired DNA methylation and gene expression data (entanglement = 0.31, cophenetic correlation score = 0.4). (**D**) Barplot indicating the number of common (black) and specific (colored) significantly up- or downregulated genes observed for each comparison versus healthy BCPs. Inner graph indicates the total number of DEGs under each condition. Venn diagram represents the number of overlapping DEGs between naive B cells and iB-ALL compared with healthy BCPs. $P < 0.001$, 1-tailed hypergeometric test. (**E**) Violin plots showing the coefficient of variation of the gene expression ($\log_2$ fold change) of the DEGs for each condition compared with healthy BCPs. $P < 0.001$ for all comparisons, 2-sided Wilcoxon's rank sum test. (**F**) Scatter plot depicting the normalized enrichment score (NES) and the contribution (represented by dot size) of particular gene modules in each group.

methylation correlated well with gene expression; hypermethylation changes were associated with gene repression, while hypomethylation changes correlated with gene activation (Figure 6, B and C). Gene expression–correlating dmCpG probes were enriched at CpG islands and distal promoters, but significantly underrepresented at open sea locations and intergenic regions (Supplemental Figure 6, A and B; statistics available in Supplemental Table 7). Moreover, the distribution of these CpG sites was associated with histone marks and chromatin states linked to active transcription (Supplemental Figure 6, C and D, and Supplemental Tables 14 and 15), identifying gene expression–associated dmCpGs in iB-ALL. For instance, hypomethylation of the CpG probe cg07893009 in iB-ALL correlated with increased expression of *LMO2* (ref. 41 and Figure 6D), while hypermethylation of the CpG probe cg06365535 was significantly associated with repression of *BRIP1* in iB-ALL (ref. 42 and Figure 6E). Additionally, reactome pathway enrichment analysis using all gene

expression–correlating dmCpG probes showed a link between gene repression and hypermethylated CpGs in *MLL*r iB-ALL, associated with impairment of cellular pathways related to cell cycle, mitosis, and DNA replication and repair (Figure 6F).

Then we sought to determine the contribution of master TFs interacting with gene expression–correlating dmCpGs. Enrichment of TFBS within these dmCpGs was performed using ELMER and publicly available human binding models from the HOCOMOCO database (43). A marked enrichment of hypermethylated CpGs was seen in SP and E2F TFs (Figure 6G). Strikingly, however, many FOS/JUN members and RUNX proteins were substantially enriched in hypomethylated CpGs, specifically for *MLL-AF4*+ iB-ALL patients, further suggesting that an epigenetic control of AP-1 members reshapes the molecular network of *MLL-AF4*+ iB-ALL.

AP-1– and RUNX-interacting factors reshape the regulatory network of iB-ALL by regulating the methylation status of downstream target
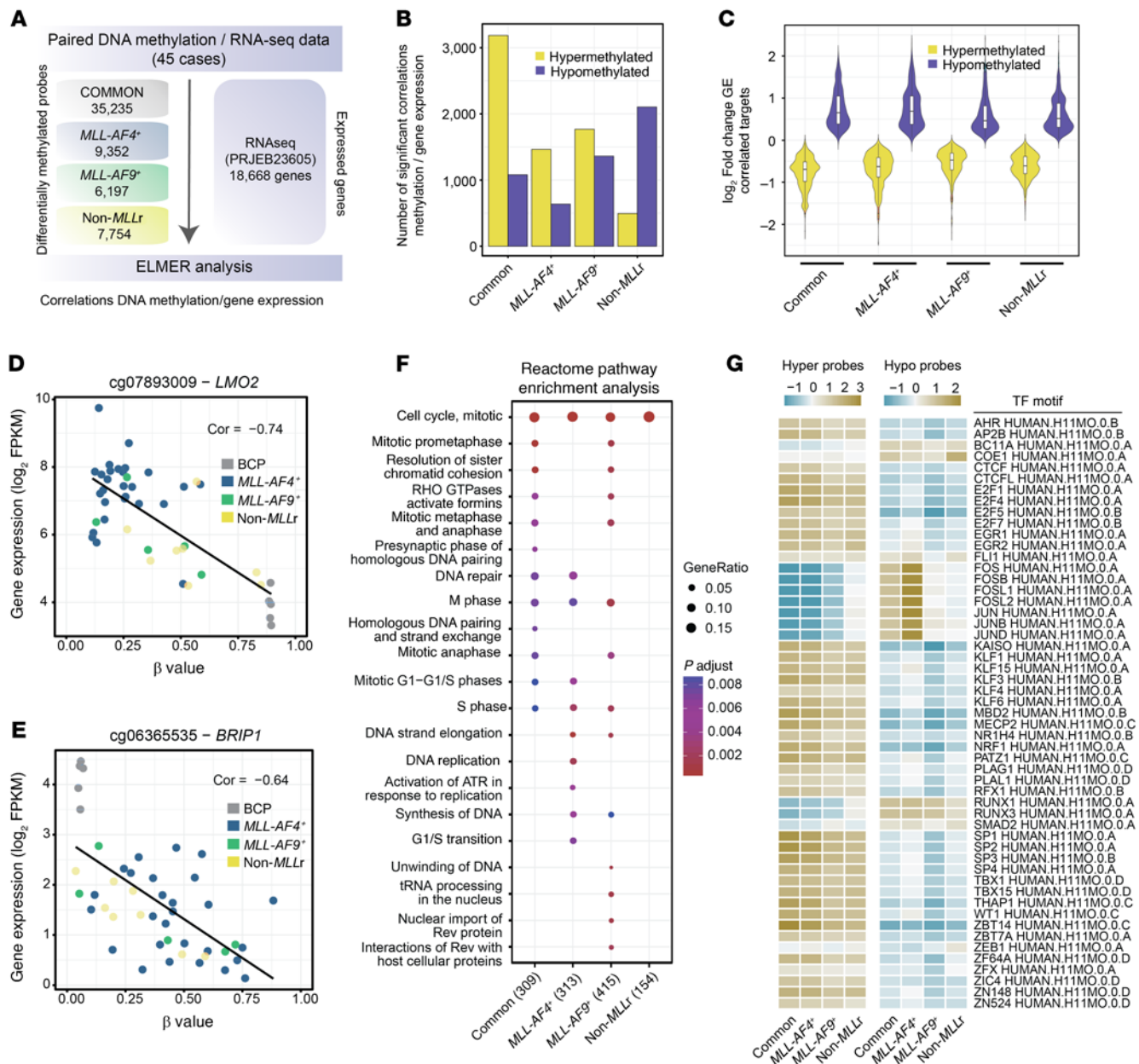
Figure 6. Integration of DNA methylation and gene expression data. (**A**) Schematic depicting the workflow for integrating DNA methylation and RNA-Seq data using the ELMER algorithm. (**B**) Barplot depicting the number of gene expression–correlating hyper- or hypomethylated CpGs (absolute Pearson's correlation > 0.5). (**C**) Violin plots showing the distribution of gene expression changes ($\log_2$ fold change of the indicated groups versus healthy BCPs) for those genes with consistent correlation with dmCpG probes. (**D** and **E**) Scatter plots indicating the correlation between DNA methylation and gene expression for the genes *LMO2* (**D**) and *BRIP1* (**E**), respectively. Pearson's correlation (Cor) score is indicated for each comparison. (**F**) Scatterplot of Reactome pathway enrichment analyses. Genes with consistent correlation with DNA methylation were used for enrichment calculation versus the background data set, which included all the genes with detectable expression in our RNA-Seq data set (18,668). Color range denotes the significance of the represented ontology (adjusted *P* value), while dot size indicates the ratio between the number of hits identified and the total number of hits in a given ontology. (**G**) Heatmap representation of enrichment of TFBSs in gene expression–correlating hyper- or hypomethylated CpGs. Color range indicates enrichment or underrepresentation of a given motif ($\log_2$ odds ratio) as calculated by the ELMER algorithm.

motifs. We next explored whether master TFs epigenetically control gene expression in iB-ALL. We first mapped the genomic context of *E2F5*, a TF enriched in hypermethylated CpG sites (Figure 6G), and found 11 highly correlated CpG probes within 1 Mbp upstream of the *E2F5* TSS (Figure 7A). This genomic region was specifically hypermethylated in iB-ALL (Figure 7B), and the E2F5 expression was repressed, particularly in *MLL-AF4*+ iB-ALL (Figure 7C).

Importantly, the average DNA methylation of E2F5 motifs substantially increased in *MLL-AF4*+ iB-ALL (Figure 7D), suggesting that the absence of E2F5 facilitated methylation at these particular loci. Furthermore, the expression of E2F5 targets was below that expected by chance in all iB-ALL groups (Figure 7E). As expected, the expression of E2F5 targets was also repressed in naive B cells, as E2F5 is a transcriptional repressor in terminally differentiated B cells.
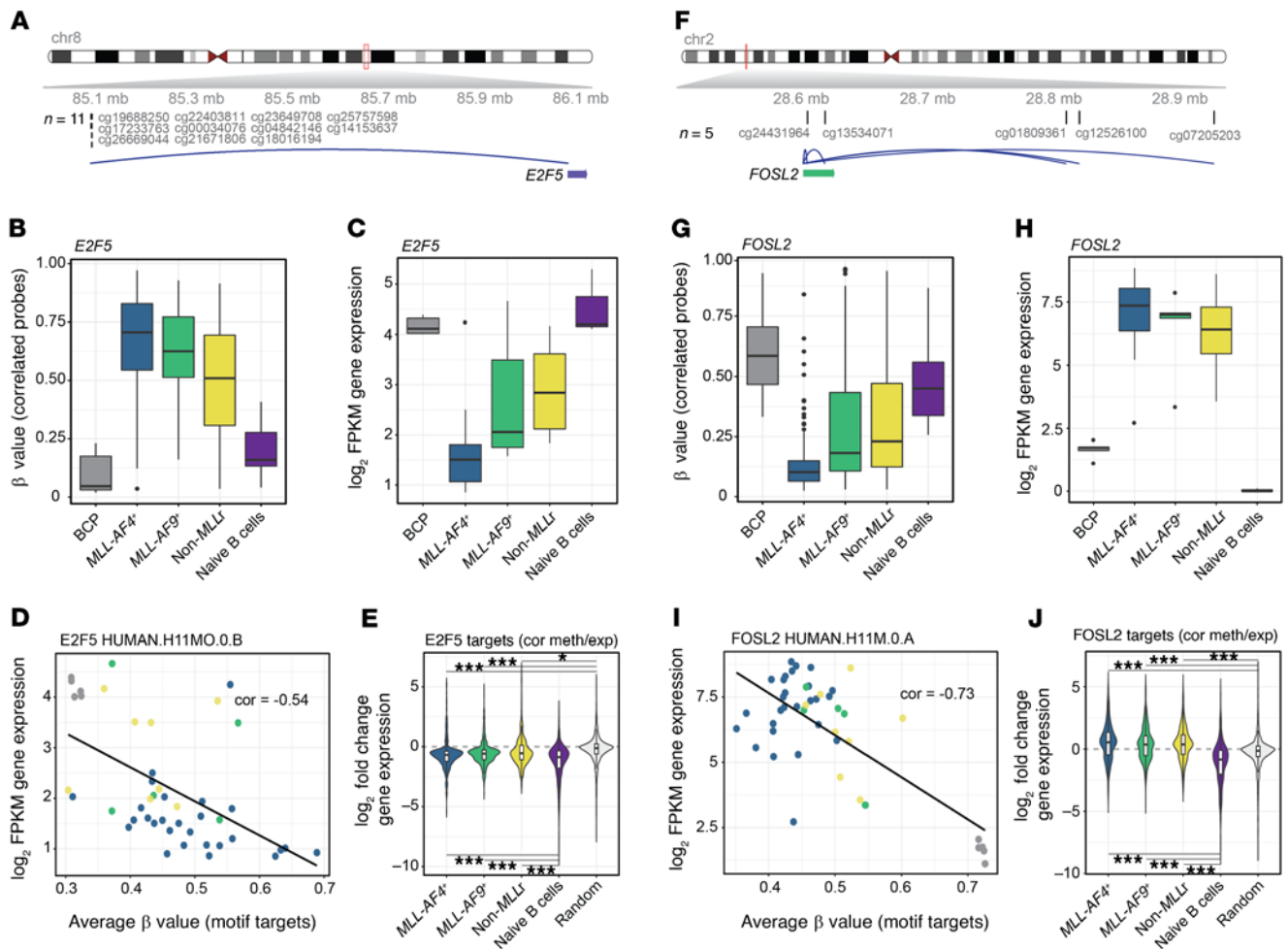
Figure 7. E2F and AP-1 interacting factors control the methylation status of downstream target motifs. (**A**) Ideogram representing the genomic location of *E2F5* expression–correlating dmCpG sites. *n* denotes the number of correlating dmCpGs identified with ELMER algorithm. (**B**) Boxplot depicting the average methylation of the significant *E2F5* expression–correlating CpG probes across different groups. (**C**) Boxplot reflecting the expression of *E2F5* in the indicated groups. (**D**) Scatter plot showing the correlation between average DNA methylation of E2F5 motif targets and the expression of *E2F5*. Colored dots: blue, BCP; red, *MLL-AF4+*; green, *MLL-AF9+*; yellow, non-*MLL*r. (**E**) Violin plots indicating the distribution of gene expression changes (log$_2$ fold change of the indicated groups versus healthy BCPs) of target genes with E2F5 motifs obtained with ELMER algorithm.*$P < 0.05$; ***$P < 0.001$, 2-sided Wilcoxon's rank sum test. All correlated genes with E2F5 motifs included in any of the iB-ALL subgroups were used for the representation of the B cell gene expression distribution. The "random" group includes a random sampling of the same number of genes included in the B cell group, but using the original gene expression matrix including all genes with detectable expression in the RNA-Seq data set. (**F**–**J**) Same as **A**–**E**, but for the TF FOSL2.

Then we focused on AP-1 members, which were highly enriched at hypomethylated CpG sites in *MLL-AF4+* iB-ALL (Figure 6G). Five highly correlated enhancer-linked CpG probes were found distributed across 0.35 Mbp downstream of the *FOSL2* promoter (Figure 7F). These dmCpG loci were robustly demethylated in iB-ALL, especially in *MLL-AF4+* patients (Figure 7G). Hypomethylation of such dmCpGs was accompanied by a significant increase in *FOSL2* expression in iB-ALL (Figure 7H). Accordingly, the average DNA methylation of binding motifs dramatically decreased in iB-ALL, particularly in *MLL-AF4+* patients (Figure 7I), and the expression of FOSL2 targets in iB-ALL was higher than in naive B cells and that expected by chance in iB-ALL (Figure 7J).

To confirm that FOSL2 plays a role in reshaping the epigenetic landscape of iB-ALL, we performed a deeper network analysis to validate the link between the expression of FOSL2 target genes and highly correlated CpGs. Top network nodes were characterized by the presence of hypomethylated FOSL2-binding motifs and upregulation of corresponding FOSL2 targets (Supplemental Figure 7A). We further explored 2 nodes of the FOSL2 regulatory network, *DUSP10* and *CD44*, which are protumorigenic genes highly expressed in iB-ALL (44, 45). *DUSP10*- and *CD44*-related dmCpGs were significantly hypomethylated (Supplemental Figure 7, B and C) and *DUSP10/CD44* inversely overexpressed in iB-ALL, particularly in *MLL*r iB-ALL (Supplemental Figure 7, D and E).

In order to demonstrate the functional impact of FOSL2 upregulation in the methylation status of *MLL-AF4+* leukemias, we performed functional assays in CRISPR-Cas9–mediated FOSL2 knockout *MLL-AF4+* SEM cells (Figure 8A). Overall, we observed a significant global hypermethylation of the genome upon FOSL2 ablation (Figure 8B), and a total of 12,218 hypermethylated and
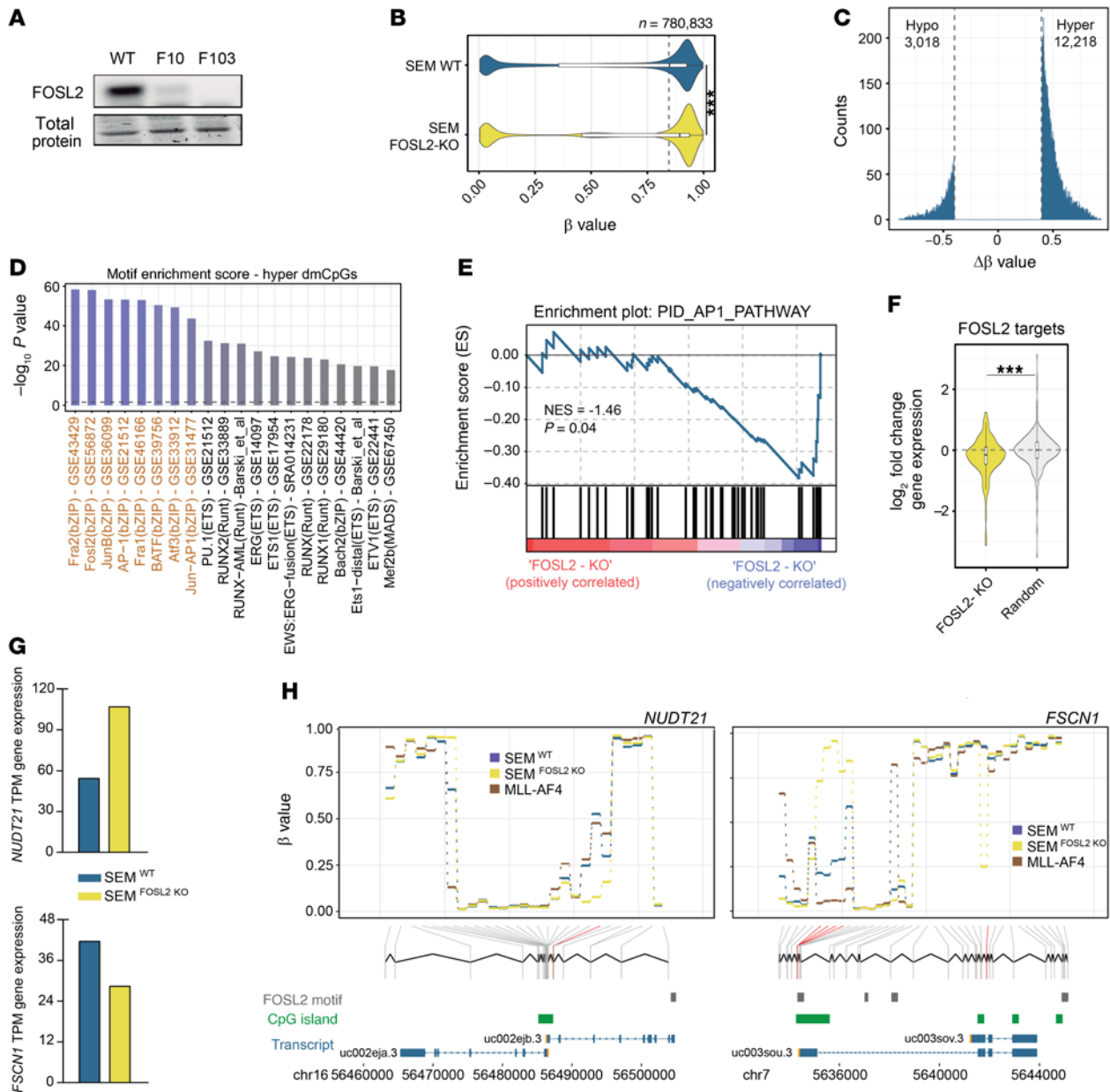
Figure 8. FOSL2 contributes to the modulation of the *MLL-AF4*+ methylome. (**A**) Western blot confirming FOSL2 knockout in 2 clones of CRISPR/Cas9-edited SEM cells. Total protein refers to the loading control measured by Ponceau staining. (**B**) Violin plot displaying the average methylation landscape of SEM-WT and SEM-FOSL2^{KO} cells ***$P < 0.001$, 2-sided Wilcoxon's rank sum test. (**C**) Histogram indicating the number of hyper- and hypomethylated CpG sites between SEM-FOSL2^{KO} and SEM-WT cells (mean β difference > 0.40). (**D**) HOMER motif enrichment analysis highlighting the top enriched TFBS identified in the context of hypermethylated CpGs in SEM-FOSL^{KO} cells. (**E**) Plot illustrating the enrichment analysis obtained from gene expression data from SEM-FOSL2^{KO} and SEM-WT and the gene set corresponding to the AP-1 pathway. The NES and the significance scores were calculated using the preranked mode of GSEA. (**F**) Violin plots displaying the distribution of gene expression changes (log$_2$ fold change of SEM-FOSL2^{KO} versus SEM-WT cells) of FOSL2 target genes (number of annotated dmCpGs > 3, $n = 107$) or a random subset on genes ($n = 500$), including all genes with detectable expression in the RNA-Seq data set. ***$P < 0.001$, 2-sided Wilcoxon's rank sum test. (**G**) Barplots representing RNA-Seq expression results (in FPKM) of *NUDT21* and *FSCN1* genes in a pool of SEM-WT and SEM-FOSL2^{KO} cells. (**H**) Plots depicting the genomic localization and β value score of the interrogated MethylationEPIC probes in the vicinity of *NUDT21* and *FSCN1* genes. Colors denote the methylation landscape of the indicated groups, and MLL-AF4+ iB-ALL patient samples were included for proper comparisons. Significant dmCpGs (mean β difference > 0.40) are highlighted in red. Bottom panel displays the genomic context of the aforementioned probes and genes, including the location of FOSL2 motifs (GTRD database) and CpG islands. TSSs are highlighted in orange.

3018 hypomethylated sites were identified between FOSL2^{KO} and SEM WT cells (Figure 8C and Supplemental Table 16). A subsequent HOMER motif enrichment analysis on those FOSL2-regulated dmCpGs revealed that the top significant TFBSs were mostly associated with members of the AP-1 complex (Figure 8D and

Supplemental Table 17). To further validate these observations at the gene expression level, we performed RNA-Seq in SEM WT and SEM-FOSL2^{KO} cells. We observed that genes associated with the activation of the AP-1 pathway were significantly impoverished in the context of FOSL2 depletion (Figure 8E). In addition, FOSL2

targets were significantly downregulated in FOSL2[KO] cells (Figure 8F). In the context of FOSL2 ablation in *MLL-AF4+* cells, further analyses of the FOSL2-related dmCpGs and their potential contribution to gene expression were exemplified with *NUDT21* and *FSCN1* genes (Figure 8, G and H). Upon FOSL2 ablation, a CpG island in the vicinity of *NUDT21* TSS was hypomethylated, which led to an increased expression of this 3′ end RNA cleavage and polyadenylation factor. In contrast, DNA hypermethylation of a FOSL2 motif located near the TSS of *FSCN1* was correlated with the downregulation of such genes in SEM cells. These experiments validate the role of FOSL2 observed in the in silico network approach.

We next explored the regulatory network of RUNX1 in order to expand our observations toward another classical molecular target of *MLL-AF4+* aberrantly expressed in *MLL-AF4+* iB-ALL (46). We found 4 highly correlated enhancer-linked CpG sites distributed along the genomic loci of *RUNX1* (Supplemental Figure 8A). Similar to *FOSL2*, these dmCpG loci were robustly demethylated in iB-ALL, especially in *MLL-AF4+* patients (Supplemental Figure 8B). Hypomethylation of such dmCpGs was accompanied by a significant increase in *RUNX1* expression (Supplemental Figure 8C). In addition, the average DNA methylation of RUNX1 binding motifs dramatically decreased in iB-ALL (Supplemental Figure 8D), and the expression of RUNX1 targets in iB-ALL was higher than in naive B cells and that expected by chance in iB-ALL (Supplemental Figure 8E). A network analysis of RUNX1 top target genes revealed that the RUNX homolog *RUNX2* was modulated in a similar fashion in *MLL*r iB-ALL (Supplemental Figure 8F). *RUNX2*-related CpGs were significantly hypomethylated in *MLL*r iB-ALL (Supplemental Figure 8G) and *RUNX2* inversely overexpressed in *MLL*r iB-ALL (Supplemental Figure 8H). Collectively, an intricate relationship between DNA methylation and gene expression reshapes the regulatory network of iB-ALL through master molecular hubs, such as members of the AP-1 complex and RUNX1.

MLL-AF4 regulates the expression of E2F5, AP-1, and RUNX family members. The silent mutational landscape of *MLL*r iB-ALL suggests that *MLL-AF4+* translocation may suffice to initiate leukemogenesis. To explore whether MLL-AF4 can itself activate the transcriptional program observed in iB-ALL patients, we analyzed RNA-Seq data from a recent study by Lin and colleagues that created a leukemogenic chimeric fusion between human *MLL* and murine *AF4* (18). We found that expression of *E2F5*, *FOSL2*, and *RUNX1* was similarly regulated in MLL-AF4–transduced CD34+ cells (Figure 9A) and in human primary *MLL-AF4+* iB-ALL patients (Figure 7), indicating that MLL-AF4 triggers an analogous transcriptomic rewiring in the absence of further genomic mutations. Moreover, a similar gene activation signature was observed for multiple members of the AP-1 complex, including *FOS*, *FOSL1*, *FOSB*, *JUN*, *JUNB*, and *JUND* (Supplemental Figure 9A). Of note, we found direct binding of MLL-AF4 in CD34+ cells or MLLN/AF4C in SEM cells to the promoter region of *FOSL2* and *RUNX1* (Figure 9B), *FOS*, *FOSL1*, *JUN*, *JUNB*, and *JUND* (Supplemental Figure 9B), suggesting a direct regulation of these target genes by MLL-AF4.

To validate the regulation of these targets in the context of the endogenous human translocation, we generated CRISPR/Cas9-mediated locus-specific t(4;11)/*MLL-AF4+* in CD34+ cells,

as recently reported by Secker and colleagues (47). Expression of *FOSL2* and *RUNX1* (Figure 9C), but also the other members of the AP-1 family, including *FOS*, *FOSL1*, *FOSB*, *JUNB*, and *JUND*, were upregulated upon the endogenous *MLL-AF4+* translocation event (Supplemental Figure 9C). We next performed a comprehensive analysis of the DNA methylome upon t(4;11)/*MLL-AF4+* translocation in these CD34+ cells and observed a total of 5011 hypermethylated and 6752 hypomethylated CpGs upon the induction of the translocation event (Figure 9D and Supplemental Table 18). Intriguingly, more than 80% of the dmCpG sites identified upon t(4;11)/*MLL-AF4+* induction in CD34+ cells were located at the same methylated genes affected by MLL-AF4 in iB-ALL patients, yielding an exact positional overlap of approximately 25% of CpG sites (Figure 9E). Nonetheless, AP-1 members were among the most significant TFBSs identified at t(4;11)/*MLL-AF4+* hypomethylated sites (Figure 9F and Supplemental Table 19). Collectively, MLL-AF4 controls the expression of AP-1 members in the absence of other genetic insults and is directly associated with the observed demethylation at their binding motifs, indicating that the presence of AP-1 members may protect from DNA methylation at these particular loci.

AP-1 complex sustains cell proliferation and tumorigenic capacity of MLL-AF4+ B-ALL cells in vitro and in vivo. The AP-1 complex acts as a central player in the epigenetic and transcriptional remodeling observed in *MLL*r iB-ALL patients. Thus, we were next prompted to explore in vitro and in vivo whether targeting AP-1 may represent a therapeutic opportunity for *MLL*r B-ALL. We perturbed AP-1 activity in SEM cells by either transduction of a dominant negative isoform of FOS (dnFOS) (ref. 48, Figure 10A) or CRISPR/Cas9-mediated ablation of FOSL2 (Figure 8A). dnFOS expression was impaired in in vitro cell proliferation (Figure 10A) and reduced 4-fold the clonogenic capacity of dnFOS-SEM cells (Figure 10B). In addition, tumor burden (analyzed by bioluminescence [BLI] and FACS in peripheral blood [PB] and splenomegalia analysis) was drastically reduced in xenografts transplanted with dnFOS-SEM cells in vivo (Figure 10, C–E). Even a more robust impairment in proliferation and clonogenic and tumorigenic capacity was obtained upon CRISPR-mediated FOSL2 ablation in SEM cells both in vitro and in vivo (Figure 10, F–J).

We then performed a pharmacological inhibition of AP-1 via the available chemical inhibitors SR11302 or T5224 and observed an impaired proliferation of t(4;11)/*MLL-AF4+*CD34+ cells in a dose-dependent manner (Figure 11A). To validate our observations, we expanded our in vitro pharmacological analyses of the T5224 AP-1 inhibitor in a panel of additional *MLL*r and non-*MLL*r leukemic cell lines. Of note, we confirmed a specific and dose-dependent effect of T5224 in inhibiting the proliferation of *MLL*r, but not non-*MLL*r, cell lines (Figure 11, B and C).

Finally, to validate the in vivo efficacy of our pharmacological approach, the T5224 inhibitor was combined with the B-ALL standard-of-care treatment, based on vincristine, dexamethasone, and L-asparaginase(VXL treatment), and administered to preclinical B-ALL PDX models well established in our laboratory (refs. 49, 50; Figure 12A). The levels of minimal residual disease (MRD) after 2 complete cycles of VXL and subsequent relapse rates were measured in BM, spleen, and PB. Leukemic
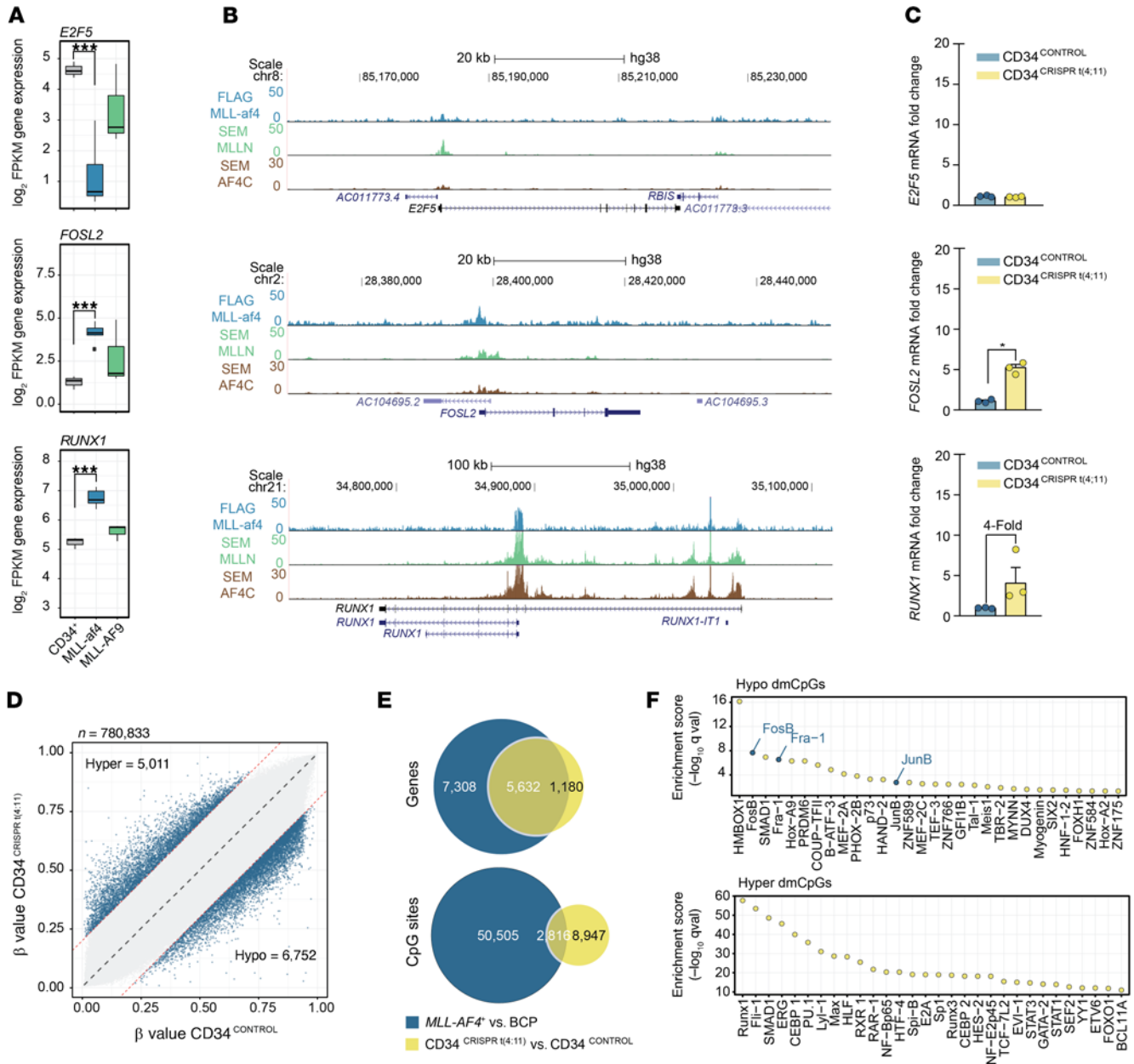
Figure 9. MLL-AF4 regulates the expression of AP-1 members and RUNX1 and reshapes the methylome landscape of CD34⁺ cells. (**A**) Boxplot depicting the average expression of *E2F5*, *FOSL2*, and *RUNX1* genes in healthy untransduced CD34⁺ cells or in CD34⁺ cells transduced with either human:murine chimeric MLL-AF4 or human MLL-AF9. ***$P < 0.001$, 2-sided Welch's *t* test. $n = 3$; $n = 6$; $n = 3$, respectively. (**B**) UCSC Genome Browser tracks representing the binding pattern of MLL-AF4 (in CD34⁺ cells) or MLLN/AF4C (in SEM cells) in the vicinity of *E2F5*, *FOSL2*, or *RUNX1* genes. Data represents ChIP-Seq signals obtained from NCBI database Gene Expression Omnibus [GEO] GSE84116 and GSE74812, respectively. (**C**) Barplots indicating RT-PCR relative fold-change of *E2F5*, *FOSL2*, or *RUNX1* expression between nonedited CD34⁺ cells (CD34^control) and CRISPR-edited CD34⁺ cells carrying locus-specific t(4;11)/MLL-AF4⁺ (CD34^CRISPR t(4;11)). Barplots represent mean± SD. *$P < 0.05$, 2-sided Welch's *t* test. (**D**) Scatterplot indicating the number of hyper- or hypomethylated CpG sites observed upon CRISPR t(4;11)/MLL-AF4⁺ edition in CD34⁺ cells (mean β difference > 0.20). (**E**) Venn diagrams representing the number of overlapping genes decorated with dmCpGs (top) or the number of overlapping dmCpGs (bottom, positional overlap) between *MLL-AF4⁺* patients and CD34⁺ t(4;11)/*M-LL-AF4⁺* (CD34^CRISPR t(4;11)) cells, as compared with healthy BCPs or nonedited CD34⁺ cells, respectively. $P < 0.001$. One-tailed hypergeometric test was used for all the comparisons. (**F**) Plots displaying enrichment of TFBS in the context of hypo- and hypermethylated CpGs in CD34⁺ t(4;11)/*MLL-AF4⁺* (CD34^CRISPR t(4;11)) cells as determined by the information obtained from the GTRD database. The y axis represents the −log₁₀ adjusted *P* value enrichment of particular TFBS data set as compared with the background distribution of the EPIC platform.

engraftment was determined before treatment in order to randomize mice based on BM leukemic burden to receive VXL or VXL+T5224 (Figure 12B). After 2 complete cycles of VXL (day 20), we observed 8 of 10 and 9 of 10 MRD negative mice (% blasts <5%) for VXL and VXL+T5224 treatment, respectively (Figure 12C). The therapeutic improvement mediated by T5224 became more evident at endpoint analysis. The proportion of mice with BM leukemic graft was lower in the T5224-treated
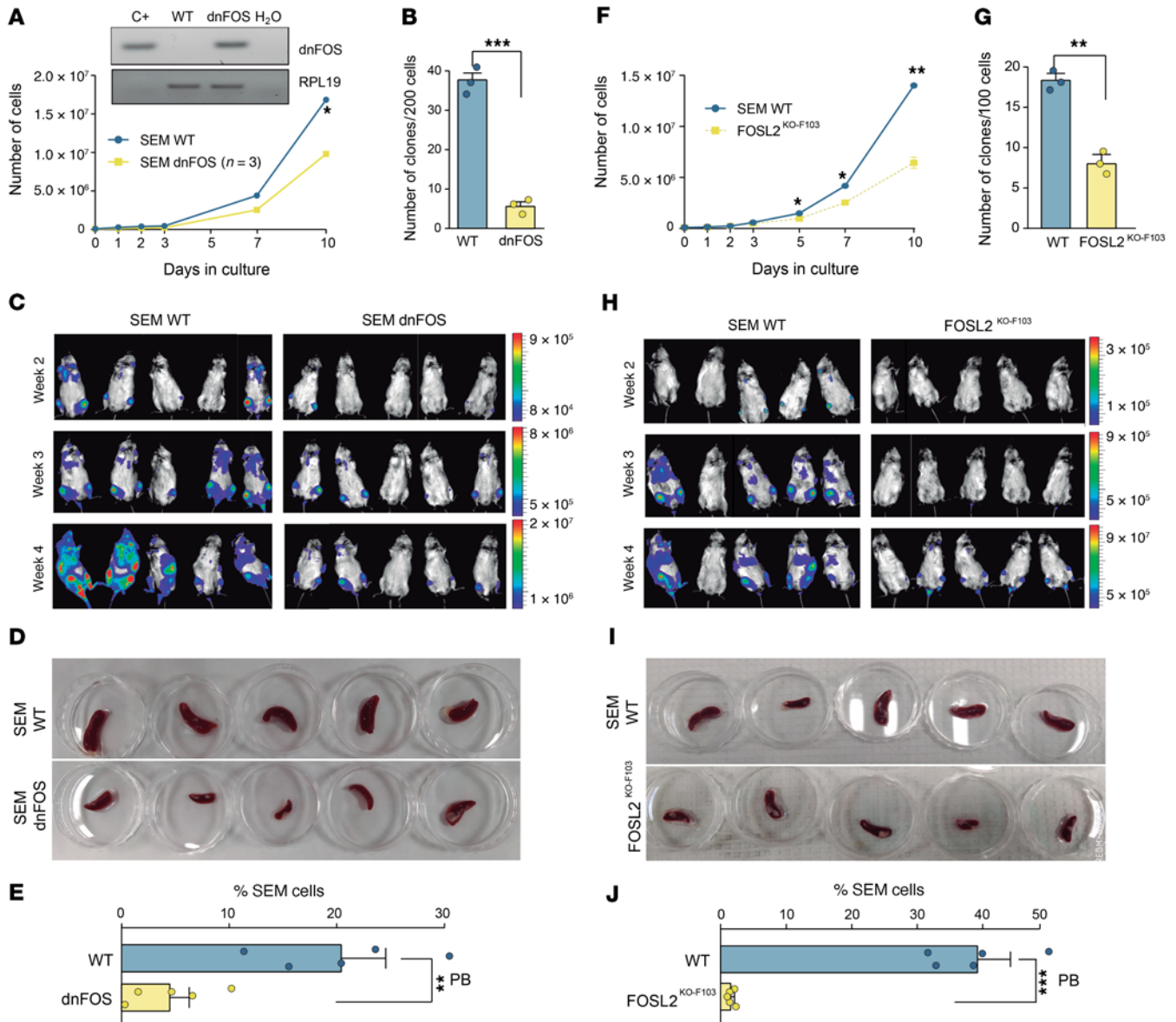
Figure 10. Targeting AP1 complex impairs the growth of *MLL-AF4*⁺ B-ALL cells in vitro and in vivo. (**A**) Impaired in vitro proliferation of dnFOS-SEM cells. A representative experiment is shown (*n* = 3). Inset represents RT-PCR confirming dnFOS expression in transduced SEM cells. RPL19 was used as a loading control. (**B**) Impaired clonogenic capacity of dnFOS-SEM cells. (**C**) BLI imaging showing significant decreased tumor burden in NSG mice transplanted with dnFOS-SEM cells in vivo (*n* = 5 mice/group). (**D**) Endpoint macroscopic images of spleens from mice transplanted with WT- and dnFOS-SEM cells. (**E**) Endpoint leukemic burden in PB of mice transplanted with WT- and dnFOS-SEM cells. (**F–J**) Same as **A–E**, but for the CRISPR-edited FOSL2^KO-F103 SEM cells. *P < 0.05; **P < 0.01; ***P < 0.001, 2-sided Welch's *t* test. Barplots represent mean±SD.

group (30% vs. 50%). Similarly, the leukemic burden in BM (16% vs. 34%), spleen (26% vs. 9%), and PB (16% vs. 3%) was consistently lower in T5224-treated mice (Figure 12D). Taken together, these results demonstrate that the AP-1 complex of TFs is central in the pathogenesis and leukemogenesis of *MLL-AF4*⁺ iB-ALL and may offer an unexplored clinical therapeutic opportunity for *MLL*r iB-ALL.

Discussion

iB-ALL, especially t(4;11)/*MLL-AF4*⁺-expressing iB-ALL, remains an outlier acute leukemia during childhood characterized by early clinical manifestation, limited response to current therapies, and

dismal outcome (2). iB-ALL is a well-established developmental cancer in which the recurrent initiating genetic/molecular alterations arise prenatally (13, 14, 51, 52). Despite improved genetically modified mouse and human xenograft models, the historical challenge to faithfully recapitulating the latency and phenotype of *MLL*r iB-ALL disease has hampered clinical/therapeutic advances. Importantly, recent elegant genome-wide DNA-Seq studies in iB-ALL revealed a silent mutational landscape regardless of *MLL* status (9, 16, 17). This together with the extremely short latency of the disease indicates that *MLL*r might be sufficient for leukemogenesis or that iB-ALL may require very few cooperating DNA mutations for overt leukemia. The nature of both the cell
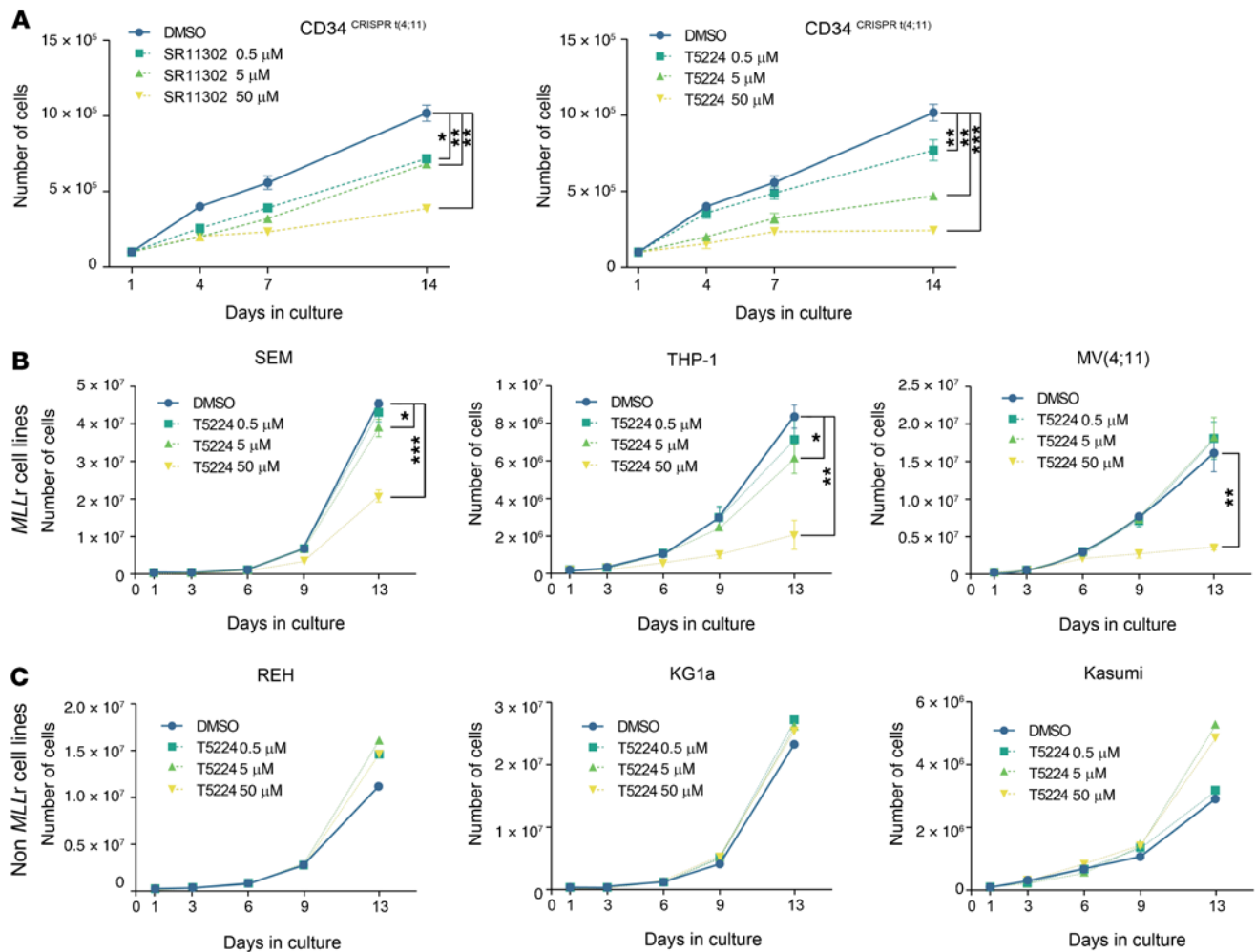
Figure 11. Pharmacological inhibition of the AP-1 complex specifically impairs the proliferation of *MLL*r leukemic cells. (**A**) Dose-dependent impaired in vitro proliferation of CD34$^{CRISPR\ t(4;11)}$ cells upon treatment with the AP-1 chemical inhibitors SR11302 (left) or T5224 (right). The DMSO condition was common for both treatments and is represented in both graphs for proper visualization purposes. (**B** and **C**) In vitro proliferation of several *MLL*r (**B**) and non-*MLL*r (**C**) leukemic cell lines treated with increasing doses of the T5224 inhibitor. Resulting *P* values were adjusted for multiple comparisons using Holm's method. *$P < 0.05$; **$P < 0.01$; ***$P < 0.001$, 1-sided Welch's *t* test. Line plots represent mean ± SD ($n = 3$), and color denotes the indicated concentration for the different drug treatments.

of origin in which *MLL*r arises and the downstream transformed hematopoietic stem and progenitor cells (HSPCs) capable of initiating leukemia and fueling disease progression is still a matter of debate (9, 23). Furthermore, in the absence of DNA mutations, other nongenetic oncogenic insults are required to initiate leukemogenesis of such aggressive leukemia in newborns (15).

In this study, we speculated that a whole-genome deconstruction of the DNA methylome landscape of this mutationally silent iBCP-ALL will likely provide unique insights into the disease pathobiology. Recent advances in computational and next-generation sequencing approaches have been crucial to uncovering the complex relationship among the genome, the epigenome, and the transcriptome of other B cell malignancies, including adult B-ALL, diffuse large B cell lymphoma (53), chronic lymphocytic leukemia (CLL) (54), and mantle cell lymphoma (55). Here, we have integrated genome-wide DNA methylome and transcriptome profiling data from a total of 69 *MLL*r and non-*MLL*r iB-ALL leukemia patients uniformly treated according to the Interfant-99/06 protocol in order to

determine the contribution of global DNA methylation to the pathogenesis of iB-ALL.

We report a global DNA hypomethylation in iB-ALL samples, similar to that found in many human tumors (56). This is supported by a recent whole-genome methylome study in leukemic twins with concordant iB-ALL who displayed a strikingly similar genome-wide methylome landscape, supportive of a convergent epigenetic evolution of the concordant iB-ALL (52). Of note, we identified that a marked proportion of the epigenetic aberrations found in iB-ALL coincided with the orchestrated changes observed during naturally occurring B cell maturation. This is consistent with previous findings in CLL (54) and other B cell neoplasms (53), indicating that regulated DNA methylation changes occurring in physiological processes, such as B cell differentiation, represent confounding noise challenging the discovery of bona fide cancer-specific methylation changes. Indeed, a reliable discrimination between the methylomes of the distinct iB-ALL subtypes was achieved by analyzing healthy BCPs and naive B cells, thus adopting a "filtered-out" strategy in which methylation changes
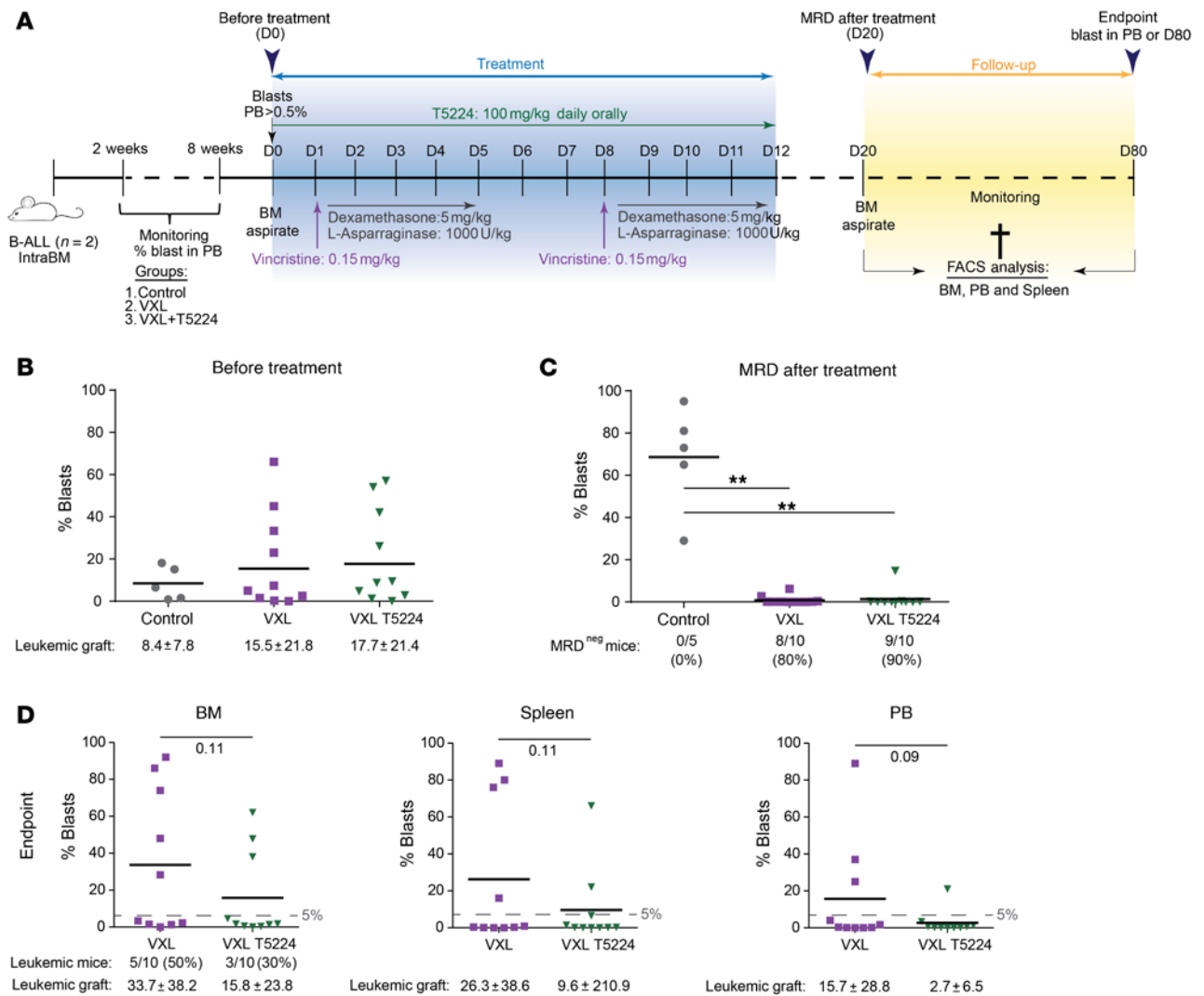
Figure 12. The AP-1 inhibitor T5224 synergistically cooperates with VXL to partially reduce leukemia aggressiveness in vivo using *MLL*r iB-ALL xenografts. (**A**) In vivo experimental design of the preclinical MLLr iB-ALL PDX models treated with VXL alone or in combination with the T5224 inhibitor. MRD was evaluated in BM 1 week after completion of the 2 cycles of VXL-based chemotherapy (day 20). Subsequent relapses were monitored in BM, spleen, and PB. (**B**) BM leukemic engraftment determined before treatment (day 0) in order to equally randomize mice based on BM leukemic burden to receive VXL or VXL+T5224 treatment. (**C**) Dot plots monitoring MRD in BM 1 week after completion of the 2 cycles of VXL±T5224 (day 20). (**D**) Proportion of leukemic mice and levels of leukemic engraftment in BM, spleen, and PB at the end of the follow-up period (mice were sacrificed when blasts were detected in PB or at day 80). For all the graphs, horizontal black line represents the mean and dots represent individual animals. **P < 0.01, 1-sided Welch's *t* test.

naturally occurring during normal B cell differentiation were subtracted, thus defining an iB-ALL–specific methylation signature.

A key aspect in the diagnosis and treatment of leukemia patients relies on the identification of common and specific alterations between defined leukemia subtypes. Here, we observed that while the aberrant DNA methylation landscape of *MLL-AF4*+ and non-*MLL*r leukemias substantially differs, *MLL-AF9*+ leukemias correlate with both *MLL-AF4*+ and non-*MLL*r subtypes. Despite the limited number of *MLL-AF9*+ cases included in this study, this observation indicates that *MLL-AF9*+ iB-ALL may display shared aberrant features and that the contribution of *MLL* rearrangement in this scenario may account for only a fraction of the observed aberrations in *MLL-AF9*+ iB-ALL. These results are in agreement with data from Stumpel and colleagues (31) showing that differential DNA

hypermethylation at promoter regions was observed between *MLL-AF4*+ and *MLL-AF9*+ patients.

Despite the intrinsic limitations of the Human Methylation EPIC platform, our study uncovers a potential association between aberrant DNA methylation in *MLL*r iB-ALL and chromatin states related to enhancer and transcriptional control of healthy hematopoietic cells, suggesting that the orchestrated molecular homeostasis of transcriptional programs key for normal hematopoiesis are epigenetically disrupted in iB-ALL. MLL protein is a H3K4 HMT found in COMPASS-like complexes, which regulate the RNA–pol II–mediated transcriptional initiation of MLL target genes (57). It is therefore plausible that the observed methylome alterations at MLL target motifs are the consequence of altered MLL activity in iB-ALL cells, in agreement with a recent study reporting DNA hypomethylation at

enhancer elements in pediatric *MLL*r B-ALL (58). Moreover, a recent study by Prange and colleagues (59) proposed that *MLL-AF4*+ and *MLL-AF9*+ fusion proteins can bind to a distinct enhancer repertoire, thus supporting the divergent distribution of altered DNA methylation patterns in these leukemia subtypes.

As none of the known DNA methyltransferases (DNMTs) have a defined sequence specificity beyond CpG sites, the establishment of aberrant, yet defined DNA methylation patterns in cancer must be achieved by other mechanisms (60). Among them, the absence of DNA methylation at given loci mediated by the steric effects of histone modifications or DNA-bound TFs could impair proper DNMT recruitment at these regions and thus may play an important role in rewiring the methylation status of iB-ALL. In this context, a mutually exclusive relationship between H3K4 modifications and DNA methylation (61) may potentially explain the differential enrichment at H3K4me3 regions observed in our analyses. De novo methylation mediated by DNMT3L is best achieved in the context of nonmethylated H3K4 (62), but binding of the DNMT3L is impeded in the presence of H3K4me (63), suggesting that H3K4 methylation may prevent de novo DNA methylation at given genomic regions. As DNA methylation changes are suggested to be a late event that coincides with loss of TF binding (64), our DNA methylation results may reflect the epigenetic rewiring driven by the relocation of multiple TFs including, but not restricted to, MLLr. A dedicated epigenetic profiling of multiple histone marks from iB-ALL samples would be of extreme relevance to further elucidating the complex relationship among DNA methylation, histone modifications, and chromatin accessibility in iB-ALL.

The comprehensive transcriptional profiling of iB-ALL cohorts allowed the identification of deregulated transcriptional programs (9, 17). Of note, differential gene expression analysis revealed that *MLL-AF4*+ iB-ALL displayed a larger expression variability, suggesting the existence of distinct molecular subgroups within *MLL-AF4*+ iB-ALL patients (9). In this context, the reciprocal fusion *AF4-MLL*+, which is expressed only in half of the t(4;11)+ iB-ALL patients, was shown to be required for expression of *HOXA* cluster genes and cooperates with MLL-AF4 to promote the emergence of hematoendothelial precursors (9, 65). Importantly, the expression of AF4-MLL/HOXA is an independent prognostic factor and identifies t(4;11)+ iB-ALL patients with improved overall and event-free survival (9).

Network-based coexpression analysis revealed the presence of predominant molecular hubs differentially altered in *MLL*r iB-ALL subtypes. We observed that FOS and JUN, members of the AP-1 family of TFs, displayed a pivotal role in the establishment of a specific transcriptional signature in *MLL*r iB-ALL, particularly in *MLL-AF4*+ patients. Indeed, components of the AP-1 complex have a well-established contribution in multiple types of human neoplasms (66), and a recent study demonstrated that FOS/JUN-related proteins are crucial players in the pathogenesis of acute myeloid leukemia (AML) (48). Further integration of DNA methylation and gene expression data, coupled with an extensive validation by multiple orthogonal approaches, confirmed that FOS/JUN proteins are not only aberrantly expressed in iB-ALL, but exert a key role in reshaping the DNA methylation landscape in iB-ALL, suggesting an intricate relationship between TF expression and the establishment of defined epigenetic programs, which

are particularly imbalanced in the context of the disease. Moreover, our integrated strategy allowed us to define specific regulatory networks by linking the functional consequence between the methylation status/expression of TFs and their downstream target genes, leading to the discovery of robust cancer cell vulnerabilities in the context of iB-ALL.

Multiple epigenetic and transcriptomic events perturb the regulatory network required for proper B cell differentiation. The identification and functional in vitro and in vivo validation of such molecular hubs deregulated in *MLL*r iB-ALL, including the AP-1 axis, provide insights toward a better understanding of the pathogenesis and initiation of *MLL*r iB-ALL, opening up potential therapeutic avenues for *MLL*r iB-ALL through the combination of targeting approaches. Future studies should address whether the cancer cell vulnerabilities here described through a genome-wide integrative methylome-transcriptome analysis and the potential therapeutic opportunity for targeting AP-1 members in *MLL*r iB-ALL may be extended to adult *MLL*r B-ALL and *MLL*r AML.

Methods

Patients and control samples. BM samples from 69 infants (<12 months old) diagnosed with B-ALL were used in this study (percentages of leukemic blasts: 90% ± %12, range: 67%–100%). Patients were cytogenetically subgrouped into 3 groups: t(4;11)/*MLL-AF4*+ (*n* = 37), t(9;11)/*MLL-AF9*+ (*n* = 12), and without *MLL*r (non-*MLL*r B-ALL without numerical or structural chromosomal abnormalities, *n* = 20). *MLL*r was confirmed by fluorescence in situ hybridization. All patients were enrolled in the Interfant International Treatment Study (ClinicalTrials.gov NCT00015873). BM samples were collected at Erasmus MC-Sophia Children's Hospital (Rotterdam, the Netherlands), Armand Trousseau Hospital (Paris, France), and San Gerardo Pediatric Hospital (Monza, Italy). Supplemental Table 4 shows the clinic-biological features of the patients. As controls, CD34+CD19+ healthy BCPs were FACS purified from 6 human fetal livers (FLs) (18 to 22 weeks old) obtained from the MRC/Wellcome Trust Human Developmental Biology Resource Center. Samples were subjected to the Infinium HumanMethylationEPIC 850K beadchip platform (*n* = 75; *n* = 69 patients and *n* = 6 BCP controls), WGB-Seq (*n* = 8; *n* = 6 patients and *n* = 2 BCP controls), and RNA-Seq (*n* = 45; *n* = 40 patients and *n* = 5 BCP controls).

WGB-Seq, microarray-based DNA methylation analyses, and RNA-Seq experiments. Further details concerning next-generation sequencing protocols, computational pipelines, data preprocessing, and all subsequent downstream analyses are provided as Supplemental Data. This information has been also deposited at the Zenodo repository (https://doi.org/10.5281/zenodo.3695640).

Integration of DNA methylation and gene expression data. Enhancer linking by methylation-expression relationships was performed with the R/Bioconductor package ELMER (v_2.6.3; ref. 40). Methylation of DMPs from the HumanMethylationEPIC platform was correlated with expression of their 10 most proximal nearby genes to identify functional connections between the methylation status of a given region and their potential transcriptional targets. Paired DNA methylation loci-gene expression targets were identified using the supervised mode of the get.pair function (permutation size = 100000, Pe = 0.001) for hyper- or hypomethylated probes. Only classical inverse relationships between DNA methylation and gene expression were

considered to facilitate the interpretation of the results. For the identification of enriched TF motifs in the correlated gene-probe pairs, we used the get.enriched.motif function from the ELMER package with the following parameters: (a) minimum incidence = 10; (b) lower OR = 1.1; (c) minimum motif quality = BS.

ChIP-Seq for MLL-AF4–expressing CD34+ cells, and MLLN and AF4C in SEM cells. ChIP-Seq tracks corresponding to MLL-AF4 and MLLN/AF4C immunoprecipitation in CD34+ transduced cells and SEM cells were obtained from the NCBI's Gene Expression Omnibus (GEO) data sets GSE84116 (18) and GSE74812 (67), respectively. Data were processed according to Lin and colleagues (18).

SEM-dnFOS, CRISPR-generated SEM-FOSL2KO, and t(4;11)/MLL-AF4+ CD34+ cells. The SEM cell line was purchased from the DSMZ Cell Line Bank and maintained according to the manufacturer's instructions. CD34+ cells were isolated from human FL samples using the CD34 MicroBead Kit (Miltenyi Biotec), as previously described (9, 21, 68). The Flag-tagged dominant-negative FOS (dnFOS) construct was provided by Conny Bonifer (Institute of Biomedical Research, College of Medicine and Dentistry, University of Birmingham, Birmingham, United Kingdom; ref. 69). dnFOS-expressing lentiviruses were used to stably transduce SEM cells that were then FACS selected based on GFP expression (21). SEM-FOSL2KO and MLL-AF4–expressing/t(4;11)+CD34+ HSPCs were generated by CRISPR-mediated genome editing as described by our group (70) and another (47) using the Cas9 protein/tracrRNA/crRNA complex (IDT). The intronic crRNAs used for this study are listed in Supplemental Table 20.

RNA extraction, reverse transcription, real-time qPCR, and immunoblotting. RNA extraction and quantitative PCR (qPCR) were performed as previously described (71) with some modifications. Briefly, total RNA was extracted from human FL CD34+ cells or cord blood (CB) CD34+ cells using TRIzol (Sigma-Aldrich) according to the manufacturer's instructions, followed by a treatment with RNase-free DNase (Roche Applied Science). cDNA was synthesized from 1 μg total RNA using the High-Capacity cDNA Reverse Transcription Kit (Applied Biosystems). Amounts of specific mRNAs in samples were quantified by quantitative reverse-transcription PCR (qRT-PCR) using QuantStudio 7 (Applied Biosystems) and SYBR Green Master Mix (Thermo Fisher Scientific). qRT-PCR was performed in 384-well microtest plates (Applied Biosystems) with 0.5 units of Taq Polymerase (Applied Biosystems) per well and 35 to 40 cycles. In all experiments, mRNA amounts were normalized to the total amount of cDNA by using amplification signals for GUSB endogenous control. Each sample was determined in triplicate, and at least 3 independent samples of each cell lysate were used. Primer sequences and PCR conditions are listed in Supplemental Table 20. For immunoblotting, whole-cell extracts were resolved on 10% SDS-PAGE gels and blotted onto nitrocellulose membranes (Bio-Rad). Fra2 protein (FOSL2, 40 kDa) was detected with the Enhanced Chemiluminescence Detection System (GE Healthcare) using an anti-Fra2 antibody (1:1000 dilution; rabbit mAb, catalog 19967; Cell Signaling Technology).

Proliferation and clonogenic assays. SEM cells (WT, dnFOS, and FOSLKO) and t(4;11)/*MLL-AF4*+ CD34+ cells were plated at 1×10^5 cells/cm^2 in the presence of different concentrations of the AP1 inhibitors T5224 (APEXBIO) or SR11302 (TOCRIS Bioscience), and cell proliferation was assessed every 3 to 4 days. These experiments were extended using a panel of MLLr (SEM, THP-1, MV4;11) and non-MLLr (REH, KG1a, Kasumi) cell lines in the presence of different

concentrations of T5224. All cell lines were obtained from the DSMZ Cell Line Bank and genetically validated in our laboratory. To assess the clonogenic capacity of WT, dnFOS, and FOSLKO SEM, single cells were deposited into individual wells of 96-well plates using FACS-Aria Fusion Cell Sorter equipped with the Automated Cell Deposition Unit (ACDU) (BD Bioscience). Three weeks later, individual cells were scored for clonal cell expansion. The wells were inspected by light microscopy the day after cell seeding and those wells containing 2 or more cells were discarded from the analysis (65).

In vivo xenograft models for MLL-AF4+ B-ALL. Eight- to twelve-week-old NOD-Cg-Prkdcscid Il2rgtm1Wjl/SzJ (where NOD indicates nonobese diabetic) (NSG) mice (Jackson Laboratory) were bred and housed under pathogen-free conditions in the animal facility of the Barcelona Biomedical Research Park. Mice (4 to 6/condition) were i.v. transplanted with 2×10^5 Luc-GFP-expressing WT, dnFOS, or FOSLKO SEM cells, and tumor burden was monitored weekly by BLI using the Xenogen IVIS 50 Imaging System (PerkinElmer; ref. 72). SEM engraftment in PB and splenomegaly were also determined at sacrifice.

To test the efficacy of the pharmacological inhibition of AP-1 in vivo, primary MLL-AF4+ iB-ALL cells were transplanted intratibia into sublethally (2.25 Gy) NSG mice, as described (49, 50). Leukemia engraftment was monitored through weekly PB analysis, and the leukemic graft was immunophenotyped by flow cytometry. When human engraftment was more than 0.5% in PB, mice were homogeneously distributed into different groups for treatment initiation. Treatment schedules were as follows: vincristine (V, 0.15 mg/kg) once weekly intraperitoneally for 2 weeks, dexamethasone (X, 5 mg/kg), and L-asparaginase (L, 1000 U/kg) daily intraperitoneally during 5 days for 2 weeks (50). The AP-1 inhibitor T5224 (100 mg/kg) was orally administered daily for 2 weeks.

Data availability. Raw HumanMethylationEPIC data including IDAT files from naive B cells, BCPs, MLL-AF4+, MLL-AF9+ and non-MLLr iB-ALLs have been deposited in ArrayExpress (E-MTAB-8505). IDAT files from SEM-WT, SEM-FOSL2KO, t(4;11)/MLL-AF4+CD34+, and nonmanipulated CD34+ cells have been deposited in ArrayExpress (E-MTAB-10090). Raw WGB-Seq data (Fastq files) corresponding to FL-BCP and iB-ALL cases have been deposited in the European Genome-Phenome Archive (EGA EGAD00001005010). Access to WGB-Seq data will be granted upon request. RNA-Seq data have been deposited at the European Nucleotide Archive (ENA PRJEB23605) as described (9). RNA-Seq data from SEM-WT and SEM-FOSL2KO have been deposited at ENA (PRJEB42796). Other datasets and source scripts required to reproduce the content of this manuscript have been deposited at Zenodo repository (10.5281/zenodo.3695640).

Statistics. Statistical analyses were performed using R programming language and publicly available software from the R/Bioconductor and CRAN repositories. Details on the statistical methods used are provided in Results and in the figure legends of the manuscript. Detailed descriptions of additional computational analyses, including CpG island status and genomic region analyses (Supplemental Tables 6, 7, 11, 16, and 18), region set enrichment analyses (Supplemental Tables 8, 9, 10, 14, 15, and 19), integration of B cell enhancers (Supplemental Table 11), modular coexpression analyses, pathway enrichment analyses and network representation, are available as Supplemental Data.

Study approval. Human samples were collected upon informed consent and approval by the Barcelona Clinic Hospital research ethics

committee. This study was approved by the Barcelona Clinic Hospital research ethics committee (2013/8529). All animal procedures were performed in compliance with the institutional animal care committee of the Barcelona Biomedical Research Park (DAAM7393).

Author contributions

MFF, AFF, and PM conceived the study, designed experiments, analyzed and interpreted the data, wrote the manuscript, and financially supported the study. JRT designed experiments, analyzed and interpreted the data, and wrote the manuscript. CB conceived the study, designed experiments, analyzed and interpreted the data, and financially supported the study. MV, PP, AAD, IC, RTR, GFB, RFP, SLT, FGA, PSO, and IV analyzed and interpreted the data. MRO, MB, GC, PB, PS, and RWS provided clinical samples and biological data. JRT and CB have largely contributed to the manuscript in terms of computational and experimental analyses, respectively, so both deserve a shared first authorship. The final order of the authors was agreed on and approved by all the coauthors based on merit and time dedication to both data generation and data analysis and was not influenced by the race, gender, or religion of the individuals.

Address correspondence to: Pablo Menéndez, Josep Carreras Leukemia Research Institute, School of Medicine, University of Barcelona, Casanova 143, 08036 Barcelona, Spain. Email: pmenendez@carrerasresearch.org. Or to: Mario F. Fraga or Agustín Fernández, Nanomaterials and Nanotechnology Research Center, Epigenetics and Nanomedicine, Avenida de la Vega 4-6, 33940, El Entrego, Spain. Email: mffraga@cinn.es (MFF). Email: agustin.fernandez@cinn.es (AFF).

1. Downing JR, et al. The Pediatric Cancer Genome Project. *Nat Genet*. 2012;44(6):619–622.
2. Pui CH, et al. Pediatric acute lymphoblastic leukemia: where are we going and how do we get there? *Blood*. 2012;120(6):1165–1174.
3. Meyer C, et al. The MLL recombinome of acute leukemias in 2017. *Leukemia*. 2018;32(2):273–284.
4. Biondi A, et al. Biological and therapeutic aspects of infant leukemia. *Blood*. 2000;96(1):24–33.
5. Nakamura T, et al. ALL-1 is a histone methyltransferase that assembles a supercomplex of proteins involved in transcriptional regulation. *Mol Cell*. 2002;10(5):1119–1128.
6. Artinger EL, et al. An MLL-dependent network sustains hematopoiesis. *Proc Natl Acad Sci U S A*. 2013;110(29):12000–12005.
7. de Boer J, et al. In focus: MLL-rearranged leukemia. *Leukemia*. 2013;27(6):1224–1228.
8. Muñoz-López A, et al. Development refractoriness of MLL-rearranged human B cell leukemias to reprogramming into pluripotency. *Stem Cell Reports*. 2016;7(4):602–618.
9. Agraz-Doblas A, et al. Unraveling the cellular origin and clinical prognostic markers of infant B-cell acute lymphoblastic leukemia using genome-wide analysis. *Haematologica*. 2019;104(6):1176–1188.
10. Chen C-W, Armstrong SA. Targeting DOT1L and HOX gene expression in MLL-rearranged leukemia and beyond. *Exp Hematol*. 2015;43(8):673–684.
11. McLean CM, et al. The emerging roles of DOT1L in leukemia and normal development. *Leukemia*. 2014;28(11):2131–2138.
12. Krivtsov AV, et al. H3K79 methylation profiles define murine and human MLL-AF4 leukemias. *Cancer Cell*. 2008;14(5):355–368.
13. Ford AM, et al. In utero rearrangements in the trithorax-related oncogene in infant leukaemias. *Nature*. 1993;363(6427):358–360.
14. Gale KB, et al. Backtracking leukemia to birth: identification of clonotypic gene fusion sequences in neonatal blood spots. *Proc Natl Acad Sci U S A*. 1997;94(25):13950–13954.
15. Sanjuan-Pla A, et al. Revisiting the biology of infant t(4;11)/MLL-AF4+ B-cell acute lymphoblastic leukemia. *Blood*. 2015;126(25):2676–2685.
16. Bardini M, et al. Implementation of array based whole-genome high-resolution technologies confirms the absence of secondary copy-number alterations in MLL-AF4-positive infant ALL patients. *Leukemia*. 2011;25(1):175–178.
17. Andersson AK, et al. The landscape of somatic mutations in infant MLL-rearranged acute lymphoblastic leukemias. *Nat Genet*. 2015;47(4):330–337.
18. Lin S, et al. Instructive role of MLL-Fusion proteins revealed by a model of t(4;11) pro-B acute lymphoblastic leukemia. *Cancer Cell*. 2016;30(5):737–749.
19. Bueno C, et al. A human ESC model for MLL-AF4 leukemic fusion gene reveals an impaired early hematopoietic-endothelial specification. *Cell Res*. 2012;22(6):986–1002.
20. Bueno C, et al. FLT3 activation cooperates with MLL-AF4 fusion protein to abrogate the hematopoietic specification of human ESCs. *Blood*. 2013;121(19):3867–3878.
21. Prieto C, et al. Activated KRAS cooperates with MLL-AF4 to promote extramedullary engraftment and migration of cord blood CD34+ HSPC but is insufficient to initiate leukemia. *Cancer Res*. 2016;76(8):2478–2489.
22. Milne TA. Mouse models of MLL leukemia: recapitulating the human disease. *Blood*. 2017;129(16):2217–2223.
23. Ottersbach K, et al. The "never-ending" mouse models for MLL-rearranged acute leukemia are still teaching us. *Hemasphere*. 2018;2(4):e57.
24. Razin A, Cedar H. DNA methylation and gene expression. *Microbiol Rev*. 1991;55(3):451–458.
25. Jones PA, Takai D. The role of DNA methylation in mammalian epigenetics. *Science*. 2001;293(5532):1068–1070.
26. Suzuki MM, Bird A. DNA methylation landscapes: provocative insights from epigenomics. *Nat Rev Genet*. 2008;9(6):465–476.
27. Almamun M, et al. Genome-wide DNA methylation analysis in precursor B-cells. *Epigenetics*. 2014;9(12):1588–1595.
28. Nordlund J, et al. Genome-wide signatures of differential DNA methylation in pediatric acute lymphoblastic leukemia. *Genome Biol*. 2013;14(9):r105.
29. Almamun M, et al. Integrated methylome and transcriptome analysis reveals novel regulatory elements in pediatric acute lymphoblastic leukemia. *Epigenetics*. 2015;10(9):882–890.
30. Wahlberg P, et al. DNA methylome analysis of acute lymphoblastic leukemia cells reveals stochastic de novo DNA methylation in CpG islands. *Epigenomics*. 2016;8(10):1367–1387.
31. Stumpel DJPM, et al. Specific promoter methylation identifies different subgroups of MLL-rearranged infant acute lymphoblastic leukemia, influences clinical outcome, and provides therapeutic options. *Blood*. 2009;114(27):5490–5498.
32. Stumpel DJPM, et al. Hypermethylation of specific microRNA genes in MLL-rearranged infant

acute lymphoblastic leukemia: major matters at a micro scale. *Leukemia*. 2011;25(3):429–439.

33. Chillón MC, et al. Prognostic significance of FLT3 mutational status and expression levels in MLL-AF4+ and MLL-germline acute lymphoblastic leukemia. *Leukemia*. 2012;26(11):2360–2366.

34. Tejedor JR, et al. Epigenome-wide analysis reveals specific DNA hypermethylation of T cells during human hematopoietic differentiation. *Epigenomics*. 2018;10(7):903–923.

35. Yevshin I, et al. GTRD: a database of transcription factor binding sites identified by ChIP-seq experiments. *Nucleic Acids Res*. 2017;45(d1):D61–D67.

36. ENCODE Project Consortium. An integrated encyclopedia of DNA elements in the human genome. *Nature*. 2012;489(7414):57–74.

37. Roadmap Epigenomics Consortium, et al. Integrative analysis of 111 reference human epigenomes. *Nature*. 2015;518(7539):317–330.

38. Ernst J, Kellis M. Chromatin-state discovery and genome annotation with ChromHMM. *Nat Protoc*. 2017;12(12):2478–2492.

39. Bossen C, et al. The chromatin remodeler Brg1 activates enhancer repertoires to establish B cell identity and modulate cell growth. *Nat Immunol*. 2015;16(7):775–784.

40. Yao L, et al. Inferring regulatory element landscapes and transcription factor networks from cancer methylomes. *Genome Biol*. 2015;16:105.

41. McCormack MP, et al. The Lmo2 oncogene initiates leukemia in mice by inducing thymocyte self-renewal. *Science*. 2010;327(5967):879–883.

42. Levran O, et al. The BRCA1-interacting helicase BRIP1 is deficient in Fanconi anemia. *Nat Genet*. 2005;37(9):931–933.

43. Kulakovskiy IV, et al. HOCOMOCO: towards a complete collection of transcription factor binding models for human and mouse via large-scale ChIP-Seq analysis. *Nucleic Acids Res*. 2018;46(d1):D252–D259.

44. Jiménez-Martínez M, et al. The dual-specificity phosphatase 10 (DUSP10): its role in cancer, inflammation, and immunity. *Int J Mol Sci*. 2019;20(7):1626.

45. Zöller M. CD44: can a cancer-initiating cell profit from an abundantly expressed molecule? *Nat Rev Cancer*. 2011;11(4):254–267.

46. Wilkinson AC, et al. RUNX1 is a key target in t(4;11) leukemias that contributes to gene activation through an AF4-MLL complex interaction. *Cell Rep*. 2013;3(1):116–127.

47. Secker KA, et al. Inhibition of DOT1L and PRMT5 promote synergistic anti-tumor activity in a human MLL leukemia model induced by CRIS-PR/Cas9. *Oncogene*. 2019;38(46):7181–7195.

48. Assi SA, et al. Subtype-specific regulatory network rewiring in acute myeloid leukemia. *Nat Genet*. 2019;51(1):151–162.

49. Prieto C, et al. NG2 antigen is involved in leukemia invasiveness and central nervous system infiltration in MLL-rearranged infant B-ALL. *Leukemia*. 2018;32(3):633–644.

50. Lopez-Millan B, et al. NG2 antigen is a therapeutic target for MLL-rearranged B-cell acute lymphoblastic leukemia. *Leukemia*. 2019;33(7):1557–1569.

51. Bueno C, et al. Insights into the cellular origin and etiology of the infant pro-B acute lymphoblastic leukemia with MLL-AF4 rearrangement. *Leukemia*. 2011;25(3):400–410.

52. Bueno C, et al. Natural history and cell-of-origin of TCF3-ZNF384 and PTPN11 mutations in monozygotic twins with concordant BCP-ALL. *Blood*. 2019;134(11):900–905.

53. Kulis M, et al. Whole-genome fingerprint of the DNA methylome during human B cell differentiation. *Nat Genet*. 2015;47(7):746–756.

54. Oakes CC, et al. DNA methylation dynamics during B cell maturation underlie a continuum of disease phenotypes in chronic lymphocytic leukemia. *Nat Genet*. 2016;48(3):253–264.

55. Queirós AC, et al. Decoding the DNA methylome of mantle cell lymphoma in the light of the entire B cell lineage. *Cancer Cell*. 2016;30(5):806–821.

56. Ehrlich M. DNA methylation in cancer: too much, but also too little. *Oncogene*. 2002;21(35):5400–5413.

57. Wang P, et al. Global analysis of H3K4 methylation defines MLL family member targets and points to a role for MLL1-mediated H3K4 methylation in the regulation of transcriptional initiation by RNA polymerase II. *Mol Cell Biol*. 2009;29(22):6074–6085.

58. Bergmann AK, et al. DNA methylation profiling of pediatric B-cell lymphoblastic leukemia with KMT2A rearrangement identifies hypomethylation at enhancer sites. *Pediatr Blood Cancer*. 2017;64(3).

59. Prange KHM, et al. MLL-AF9 and MLL-AF4 oncofusion proteins bind a distinct enhancer repertoire and target the RUNX1 program in 11q23 acute myeloid leukemia. *Oncogene*. 2017;36(23):3346–3356.

60. Rose NR, Klose RJ. Understanding the relationship between DNA methylation and histone lysine methylation. *Biochim Biophys Acta*. 2014;1839(12):1362–1372.

61. Weber M, et al. Distribution, silencing potential and evolutionary impact of promoter DNA methylation in the human genome. *Nat Genet*. 2007;39(4):457–466.

62. Otani J, et al. Structural basis for recognition of H3K4 methylation status by the DNA methyltransferase 3A ATRX-DNMT3-DNMT3L domain. *EMBO Rep*. 2009;10(11):1235–1241.

63. Ooi SKT, et al. DNMT3L connects unmethylated lysine 4 of histone H3 to de novo methylation of DNA. *Nature*. 2007;448(7154):714–717.

64. Schoofs T, et al. DNA methylation changes are a late event in acute promyelocytic leukemia and coincide with loss of transcription factor binding. *Blood*. 2013;121(1):178–187.

65. Bueno C, et al. Enhanced hemato-endothelial specification during human embryonic differentiation through developmental cooperation between *AF4-MLL* and *MLL-AF4* fusions. *Haematologica*. 2019;104(6):1189–1201.

66. Trop-Steinberg S, Azar Y. AP-1 expression and its clinical relevance in immune disorders and cancer. *Am J Med Sci*. 2017;353(5):474–483.

67. Benito JM, et al. MLL-rearranged acute lymphoblastic leukemias activate BCL-2 through H3K79 methylation and are sensitive to the BCL-2-specific antagonist ABT-199. *Cell Rep*. 2015;13(12):2715–2727.

68. Castaño J, et al. Expression of MLL-AF4 or AF4-MLL fusions does not impact the efficiency of DNA damage repair. *Oncotarget*. 2016;7(21):30440–30452.

69. Obier N, et al. Cooperative binding of AP-1 and TEAD4 modulates the balance between vascular smooth muscle and hemogenic cell fate. *Development*. 2016;143(23):4324–4340.

70. Torres-Ruiz R, et al. Efficient recreation of t(11;22) EWSR1-FLI1+ in human stem cells using CRISPR/Cas9. *Stem Cell Reports*. 2017;8(5):1408–1420.

71. Torres R, Ramirez JC. A chemokine targets the nucleus: Cxcl12-gamma isoform localizes to the nucleolus in adult mouse heart. *PLoS One*. 2009;4(10):e7570.

72. Sánchez-Martínez D, et al. Fratricide-resistant CD1a-specific CAR T cells for the treatment of cortical T-cell acute lymphoblastic leukemia. *Blood*. 2019;133(21):2291–2304.